
SLINGBAG: SLIDING BALL ADAPTIVE GROWTH ALGORITHM WITH DIFFERENTIABLE RADIATION ENABLES SUPER-EFFICIENT ITERATIVE 3D PHOTOACOUSTIC IMAGE RECONSTRUCTION

Shuang Li*

College of Future Technology
Peking University
Beijing, China
jaeger_ls@stu.pku.edu.cn

Yibing Wang*

College of Future Technology
Peking University
Beijing, China
ddffwyb@pku.edu.cn

Jian Gao*

School of Intelligence Science and Technology
Nanjing University
Suzhou, China
ygaojiany@gmail.com

Chulhong Kim

Department of Electrical Engineering, Convergence IT Engineering, Mechanical Engineering,
and Medical Science and Engineering, Medical Device Innovation Center,
Pohang University of Science and Technology (POSTECH),
77 Cheongam-ro, Nam-gu, Pohang, Gyeongbuk 37673, Republic of Korea
chulhong@postech.edu

Seongwook Choi

Department of Electrical Engineering, Convergence IT Engineering, Mechanical Engineering,
and Medical Science and Engineering, Medical Device Innovation Center,
Pohang University of Science and Technology (POSTECH),
77 Cheongam-ro, Nam-gu, Pohang, Gyeongbuk 37673, Republic of Korea
swchoi715@postech.ac.kr

Yu Zhang

College of Future Technology
Peking University
Beijing, China
zyuai424@gmail.com

Qian Chen

College of Future Technology
Peking University
Beijing, China
chen_qian@stu.pku.edu.cn

Yao Yao**

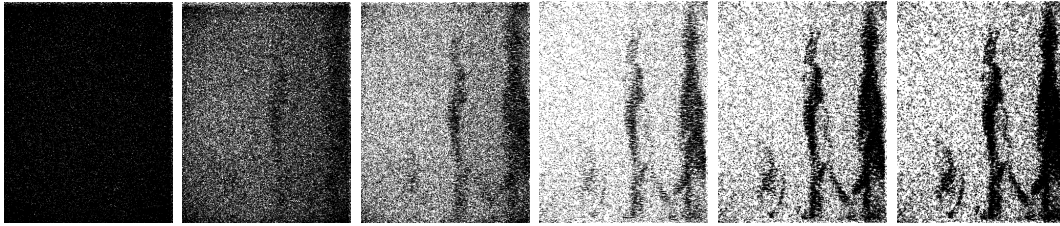
School of Intelligence Science and Technology
Nanjing University
Suzhou, China
yaoyao@nju.edu.cn

Changhui Li**

College of Future Technology
Peking University
Beijing, China
chli@pku.edu.cn

* Co-first author. ** Corresponding author.

Optimization



SlingBAG reveals finger vessels with extremely sparse sensor distribution.
Reconstruction with 238 sensors for an area of $40 \text{ mm} \times 104 \text{ mm} \times 80 \text{ mm}$ in size.

ABSTRACT

High-quality three-dimensional (3D) image reconstruction using sparsely distributed detectors or under limited view has long been a significant challenge in the field of photoacoustic (PA) imaging (PAI). Traditional iterative-based reconstruction methods suffer from both slow speed and high memory consumption for 3D PAI reconstruction. Recently, in computer graphics and computer vision, the differentiable rendering has made significant progress, particularly with the rise of 3D Gaussian Splatting. Inspired by these advancements, this work introduces these concepts into PAI reconstruction, developing a novel reconstruction algorithm: the Sliding Ball Adaptive Growth algorithm (SlingBAG) for 3D PAI reconstruction. We have demonstrated that this algorithm achieves high-quality 3D PAI reconstruction both under extremely sparse detector distributions and limited view, as well as high-fidelity quantitative PAI.

Unlike traditional reconstruction based on voxel grids in space, we established the point cloud dataset in the PAI. Each point in space represents a point source at a specific resolution (denoted by the radius of a small ball) with the corresponding initial acoustic pressure value. Besides, our approach also uses unique differentiable rapid radiator based on the spherical decomposition strategy and the randomly initialized point cloud adaptively optimized according to sparse sensor data. Each point undergoes updates in its 3D coordinates, initial pressure, and resolution (sphere radius). Points undergoes adaptive growth during iterative process, including point destroying (if they have excessively low pressure or resolution), point splitting (if their resolution is too high), and point duplicating along the gradient of their position, manifesting the sliding ball effect. This carefully designed strategy not only improves the reconstruction accuracy, but also helps reduce the computational resource usage, making our method very efficient.

Finally, the point cloud-to-voxel grid shader based on our physical model renders the final reconstruction results. Simulation data and real data reconstruction results demonstrate that the SNR of our SlingBAG reconstruction result can reach more than 40 dB under extremely sparse sensor distribution, while the SNR of the reconstruction result by traditional back-projection algorithm is less than 20 dB under the same condition. Moreover, the result of SlingBAG's structural similarity to the ground truth acoustic source is significantly higher, with an SSIM value of 95.6%. In cases where traditional algorithm reconstruction results are nearly indistinguishable between source and artifacts, the PA signal in new sensor positions simulated from the SlingBAG algorithm reconstruction result, exhibited over 80% structural similarity to the real sensor signal, achieving quantitative photoacoustic reconstruction under extremely sparse sensor distributions.

Notably, our differentiable rapid radiator can also be used for forward PA simulation in homogeneous, non-viscous media, with substantial increase in speed over current methods that numerically simulate the wave propagation, such as k-Wave. The dataset and all code will be open source, including GPU-accelerated code based on Taichi and pure CUDA syntax.

Keywords Differentiable radiation · iterative 3D PA reconstruction · computer graphic pipeline · sparse sensor distribution

1 Introduction

In recent years, three-dimensional (3D) photoacoustic imaging (PAI) based on the 2D matrix array has gained rapid development and shown enormous potential in *in vivo* imaging, including human peripheral vessel imaging and small animal imaging. High-quality 3D reconstruction with sparsely arranged sensors has consistently been a significant challenge in the field of photoacoustic imaging. Researchers have developed various array configurations, such as spherical [1, 2, 3, 4, 5] and planar arrays [6, 7, 8], and have also employed synthetic planar arrays through scanning of non-focused linear arrays to achieve 3D photoacoustic imaging [9]. However, high-quality 3D PAI based on traditional back-projection reconstruction algorithms demands not only very dense sensor configurations to meet the Nyquist sampling criterion but also full-view acquisition, leading to extremely high cost and complexity of system development or significant time costs associated with synthetic arrays that requires scanning [10]. In reality, sparse array elements are generally employed considering the cost and image time. Although back-projection based reconstruction methods are widely employed for PAI, when the sensor arrays are sparse or cover an incomplete view, the missing spatial phase data causes multiple artifacts, including ring artifacts and radial artifacts, as well as poor signal-to-noise ratio (SNR), which greatly hinders the morphological evaluation of vasculature and tissues as well as the application of quantitative photoacoustic imaging.

To meet this challenge, scholars have explored traditional iterative reconstruction (IR) methods to perform 3D image reconstruction of arrays with sparse detectors or limited view. Although the IR method, serve as enhanced and refined technology to direct and analytical reconstruction, significantly enhancing the quality of reconstructed images under non-ideal imaging conditions, the high time costs and computer memory consumption for 3D PAI reconstruction severely hinder the feasibility of these iterative approaches [11, 12, 13]. In addition to traditional iterative methods, many researchers have leveraged deep learning to achieve 3D reconstruction from sparse arrays [14, 15, 16]. However, these approaches often require large datasets to train the networks, resulting in substantial training time costs. Moreover, the networks trained through these methods often lack generalizability, meaning the networks trained on one system cannot be used for reconstructing for other PAI systems.

The field of 3D computer vision shares a similar challenge with photoacoustic imaging: 3D reconstruction and novel view synthesis from sparse viewpoints. Recent advances in differentiable rendering technologies such as NeRF [17], InstantNGP [18], TensoRF [19] and 3D Gaussian Splatting [20] have provided many breakthroughs. Researchers in the photoacoustic imaging domain have attempted to use NeRF for photoacoustic image reconstruction [21]. However, neural radiance fields are voxel-grid-intensive representations that map grid positions to physical information using multi-layer perceptrons (MLPs). These methods rely on ray tracing to sample the neural field along rays, then train the network on the sampled parts, which is highly time-consuming and inefficient. In photoacoustic imaging particularly, the sampling process is even more complex. It requires creating a spherical shell with a certain thickness by calculating the propagation distance corresponding to the sensor temporal signals and sampling the neural field using this shell. Such computational demands are almost untenable for 3D PAI, limiting current research primarily to two-dimensional (2D) photoacoustic tomography.

In 3D Gaussian Splatting, the scene is represented as discrete 3D Gaussian ellipsoids, each assigned opacity and spherical harmonics. The 3D Gaussian ellipsoids are projected onto a 2D scree, and alpha blending is applied to the sorted 2D Gaussians to render the image. The difference between the rendered image and the observed image serves as the loss function. By minimizing the loss function, it optimizes the distribution and physical parameters of the Gaussian ellipsoids, achieving high-quality and high-speed 3D reconstruction from sparse viewpoints with low memory consumption.

Inspired by 3D Gaussian Splatting, we propose the Sliding Ball Adaptive Growth algorithm (SlingBAG) for 3D PA image reconstruction, storing PA source information in the form of point clouds rather than voxel grids and performing iterative reconstruction. Besides, in this work, the calculation of PA signal is fully differentiable through our differentiable rapid radiator. Therefore, the PA signal is the superposition from signals by a collection of discrete points in space, each associated with acoustic pressure and size (represented by the radius of a sphere). Using a physics-based PA forward model via our differentiable rapid radiator, we synthesize the received PA signals from these discrete point clouds by the sensors. By minimizing the difference between the synthesized and the observed sensor signals, we optimize the discrete points, and convert the optimized point cloud into a voxel grid based on our physical model, thereby efficiently achieving high-quality 3D reconstruction.

We present a detailed and comprehensive description of the SlingBAG algorithm, including its core differentiable rapid radiator, point cloud optimization, and the physics-based point cloud-to-voxel grid shader. To validate our method, we successfully employed SlingBAG to realize large-scale 3D PAI images reconstruction from both simulated data and *in vivo* animal experiment data under sparse sensor distributions. Our high-quality imaging results shows superior power of this iterative reconstruction method.

2 Related works

2.1 Iterative-based photoacoustic imaging reconstruction

In reality, PA signal detection is often conducted in non-ideal imaging scenarios such as limited view, sparse view, finite bandwidth, and acoustically heterogeneous media. These imperfect imaging conditions reduce the image accuracy and quality for back-projection based reconstruction algorithms. In 2002, Paltauf et al. [22] developed an iterative reconstruction technique designed to improve the quality of images obtained from incomplete photoacoustic (PA) projections. This advanced IR method reconstructs PA images by iteratively minimizing the difference between the observed and simulated projections, thereby improving the accuracy and clarity of the resulting images. Subsequently, more IR methods have been developed because they can incorporate various physical imaging factors into the reconstruction model. In 2012, Kun Wang et al. [11] attempted to enhance the image quality of three-dimensional photoacoustic computed tomography (3D PACT) using the then-advanced iterative image reconstruction algorithms. They implemented and studied two iterative reconstruction methods for 3D photoacoustic tomography (PAT) small animal imaging: the penalized least squares (PLS) method with quadratic smoothing penalty and the PLS method with total variation (TV) norm penalty. Their work employed a hand-written discrete-time frequency domain imaging model as the forward process and a rotating semi-ring system, resulting in significant time costs, with each iteration time lasting over four hours. In 2013, Chao Huang et al. [23] developed optimized forward and back-projection operators based on the k-space pseudospectral method to numerically solve the PA wave equation in the time domain. This method remained slow and required substantial memory, heavily dependent on the reconstruction region grid and time steps, thus limiting the performance of PACT imaging systems.

In 2016, Simon R. Arridge et al. [24] provided a simple mathematical derivation of the PA forward operator adjoint from physical, theoretical, and numerical perspectives in a continuous framework. They described and demonstrated an efficient numerical implementation of the adjoint operator using the k-space time-domain wave propagation model. That same year, they used this adjoint operator with compressed sensing techniques, employing random, incoherent encoding of PA signals and sparse-constrained image reconstruction enhanced by Bregman iteration to accelerate high-resolution 3D PACT [25]. Due to the significant computational and memory consumption, their 3D imaging attempts were limited to a voxel count of the order of 10^6 . Additionally, their time-domain data utilized ultra-high bandwidth probes, which do not align with the mid-to-low frequency ultrasound probes commonly used in current PACT imaging systems for deeper imaging. In 2018, Andreas Hauptmann et al. [14] introduced an iterative algorithm combined with deep neural networks, primarily using gradient information fitted by neural networks to compensate for limited view artifacts. Their method was sensitive to small perturbations in the forward process and often requiring retraining. The generalizability was also limited, as the method required a large amount of training data, making it costly and prone to overfitting to a specific system, thereby hindering transferability. In 2019, Ruibo Shang et al. [12] constructed the imaging system's forward model using directly measured graphite point source signals and proposed an optimization method based on sparse matrices. Due to the low optimization efficiency and the large scale of the system matrix, the processing time remained long, and the reconstruction quality did not show a significant advantage due to the inaccurate forward model.

Most recently, in 2023, Jiaqi Zhu et al. [13] comprehensively compared model-based iterative reconstruction methods that minimize the least squares criterion using different regularization terms, regularization parameters, and optimization algorithms. They employed computer simulations, experimental phantoms, *ex vivo*, and *in vivo* data, particularly addressing the limited view problem in photoacoustic tomography for a planar detection geometry. It was evident that reconstructing large-field 3D PACT images using iterative methods remains challenging, sensitive to parameters, and requires additional computational costs. Their work was still limited to a spatial voxel count of the order of 10^6 , and the most effective method, TV+Bregman, still took over four hours in total. The authors also mentioned that iterative methods are currently impractical for high-resolution 3D imaging involving a large number of voxels. They are more suitable for smaller datasets related to 2D PACT. Furthermore, iterative methods entail a flexibility trade-off, as the model matrix must be precomputed for a specific set of imaging parameters. If these parameters change, the matrix must be recomputed at significant computational costs.

Although those approaches effectively suppress image artifacts caused by noisy and incomplete data through the use of regularization techniques, however, IR reconstruction still requires repeatedly calculating PA forward and backward models, which imposes a significant computational burden, especially for 3D imaging. Additionally, traditional IR algorithms demand substantial memory, posing a considerable challenge when deployed on GPU for acceleration. Although IR can directly reconstruct the region of interest, its memory requirements remain substantial.

2.2 Differentiable rendering

In recent years, differentiable rendering technology has become a popular topic in the computer vision and computer graphics communities [26, 27, 28, 19, 29]. This technology enables self-supervised reconstruction of 3D scenes

directly from scene observations, usually multi-view images. The photo-metric difference between the rendered image generated by the differentiable rendering pipeline and the actual captured image is utilized as a loss function, guiding the reconstruction of the entire scene through gradient back-propagation.

With advancements in this field, scene representation has shifted from implicit to explicit, accompanied by a progression from heavy neural network architectures to lightweight ones, or even none at all. Neural Radiance Field (NeRF) [17], a well-known method, employs multi-layer perceptrons (MLPs) to map 3D spatial positions and viewing directions to colors and density. Then a differentiable volume rendering technique is employed to integrate these values along the rays, generating rendered pixels. MLPs are optimized by minimizing the error between rendered and observed pixels, reconstructing the scene as an implicit radiance field. However, NeRF’s reliance on dense sampling and complex MLP networks results in slow optimization, often requiring several days. The following Plenoxels [30] utilizes a sparse voxel grid with learnable spherical harmonics to represent the 3D scene. By interpolating the spherical harmonic coefficients across the grid, Plenoxels determine the colors of sampled points on the rays. These colors are then integrated into pixels with differentiable volume rendering. Notably, Plenoxels operates without a network structure, ensuring highly efficient scene reconstruction. For efficient and high-quality reconstruction, InstantNGP [18] divides the 3D scene into multi-scale grids, stores learnable features on each cell with hash coding. When sampling along a ray, features at each sample point are obtained through grid interpolation. These features are then transformed into color and density using a shallow MLP. Finally, these sample points are integrated into pixels through volume rendering.

The above method relies on ray tracing, involving sampling along each ray’s path. The training is performed on limited random rays and thus efficient. However, image rendering requires densely sampling every ray emitted by every pixel, leading to sub-optimal efficiency. Recently, the emergence of 3D Gaussian Splatting (3DGS) [31] has addressed this issue. 3DGS employs object-order rendering, implements a high-quality and efficient reconstruction through differentiable tile-based rasterization pipeline and real-time rendering is achieved. The scene is represented as discrete 3D Gaussian ellipsoids, each assigned opacity and spherical harmonics. The 3D Gaussian ellipsoids are projected onto a 2D screen using Elliptical Weighted Average (EWA) [32], and alpha blending is applied to the sorted 2D Gaussians to render the image. The difference between the rendered image and the observed image serves as the loss function, and the position, size, orientation, opacity, and spherical harmonics of the 3D Gaussian ellipsoids are optimized. Additionally, the backward gradients guide the adaptive cloning and splitting of the Gaussian ellipsoids, ensuring high-quality scene reconstruction.

Inspired by recent research on differentiable rendering, we make the photoacoustic forward process fully differentiable to achieve high-quality 3D reconstruction in a self-supervised manner. We represent the acoustic source signal as a series of discrete points in space, with each point having an associated acoustic pressure and resolution (represented by the radius of the sphere). Then, using a physics-based photoacoustic imaging forward process, we synthesize the signals from these discrete points into signals received by the sensors. By minimizing the difference between the synthesized and the actual observed sensor signals, we optimize the discrete points, thereby efficiently achieving high-quality 3D reconstruction.

3 Method

3.1 Differentiable Rapid Radiator Based on Multi-Order Spherical Decomposition

In the field of computer graphics, rendering describes the forward process of converting the shape, color, and material of a three-dimensional scene into a two-dimensional image. Conversely, reconstruction is the inverse process that restores three-dimensional scene shape, color, and material from two-dimensional images. Differentiable rendering, characterized by its differentiable rendering process, enables the computation of image gradients and the optimization of three-dimensional scene parameters through methods like gradient descent, further facilitating the restoration of 3D scenes. Differentiable rendering is foundational for high-quality 3D scene rapid reconstruction technologies such as NeRF and 3D Gaussian splatting. The rendering equation used in light rendering simulates the propagation of light within a scene based on edge sampling Monte Carlo path-tracing methods. However, the acoustic radiation process in photoacoustic imaging differs significantly.

Corresponding to 3D vision, the forward process in photoacoustic imaging describes the propagation of ultrasound waves from photoacoustic signal sources with initial photoacoustic pressure to the transducer’s reception, resulting in temporal acoustic signals. The inverse process reconstructs the initial photoacoustic pressure at the acoustic source from these received temporal signals. Since the initial photoacoustic pressure is proportionate to the light absorption coefficient of the source, the distribution of the initial photoacoustic pressure can be considered a morphological feature of the light-absorbing tissue.

K-Wave [33] is a widely used simulation toolkit in the photoacoustic imaging field. It numerically solves the wave equation using the pseudo-spectral method to obtain temporal pressure signals at all grid space positions from the initial acoustic pressure of the sources. This method provides high simulation accuracy and supports extensive application scenarios by allowing settings for various medium acoustic properties. However, this method requires substantial storage space when a large-scale grid is used to contain the acoustic source and sensor array, which makes it challenging for researchers to apply this simulation toolkit in 3D reconstruction methods. Additionally, the forward propagation process using the pseudo-spectral method does not support direct gradient back-propagation, limiting its application in iterative reconstruction methods.

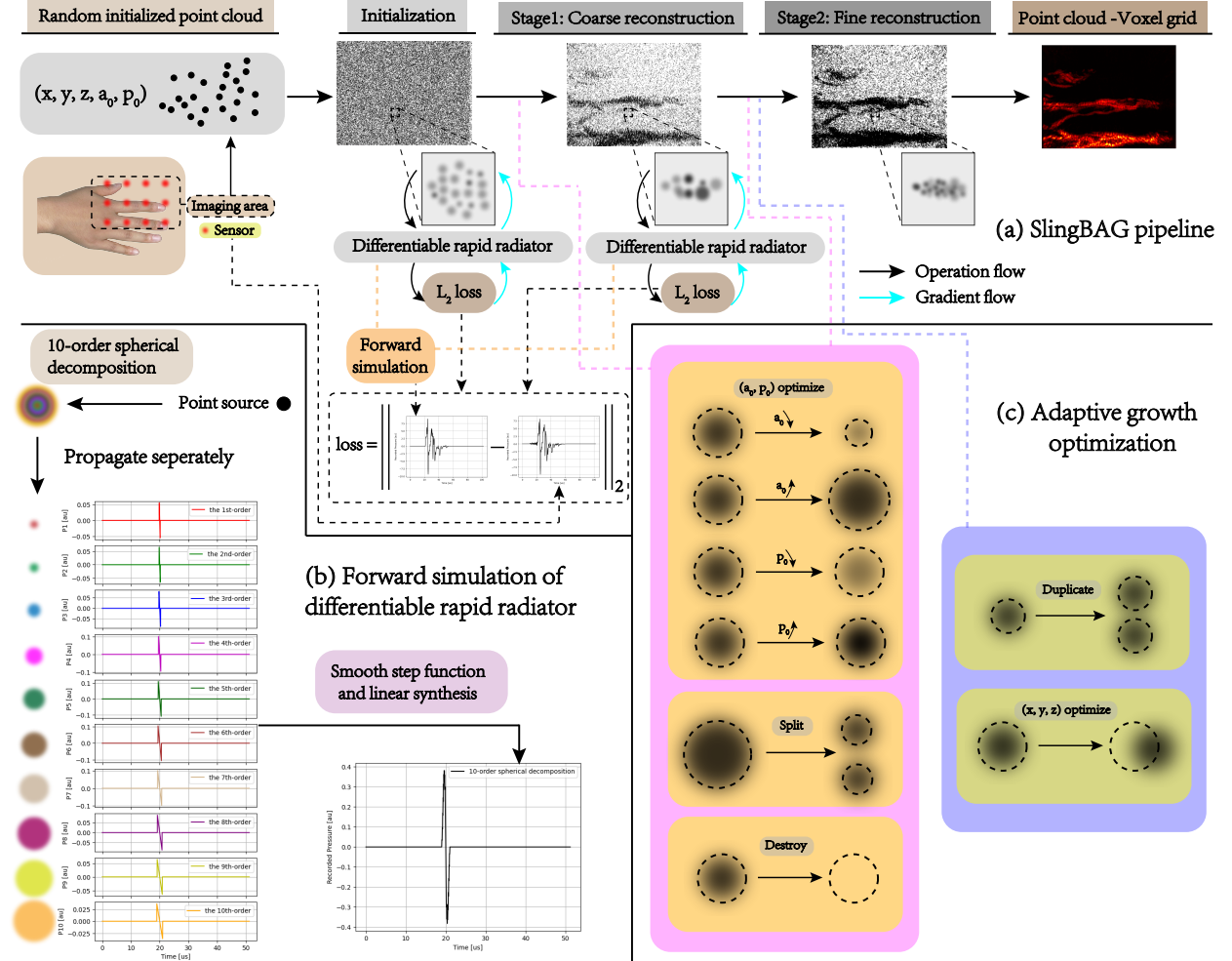


Figure 1: The overview framework of Sliding Ball Adaptive Growth algorithm. (a) The SlingBAG pipeline. (b) The forward simulation of differentiable rapid radiator. (c) Adaptive growth optimization based on iterative point cloud.

Inspired by differentiable rendering from computer graphics, and based on the principles of photoacoustic imaging, we propose the concept of "differentiable acoustic radiation" and introduce the first differentiable rapid radiator in the photoacoustic imaging field. This model can be a better alternative compared to k-Wave for simulating the propagation of initial acoustic pressure in homogeneous, non-viscous media at any spatial scale. The process is entirely differentiable and GPU-friendly, which is also quantitatively compared with k-Wave simulation results with more than 99.5% similarity but ten thousands of times faster. This radiation model views the acoustic radiation process of a point acoustic source with initial pressure p_0 at spatial coordinates (x_s, y_s, z_s) and resolution a_0 as the superposition of acoustic radiation from multiple small spheres with different radii and uniformly distributed initial acoustic pressures, which is called multi-order spherical decomposition. We display the forward simulation of our differentiable rapid radiator in Fig. 1(b).

(i) **Forward Simulation.** For a point source with resolution a_0 , spatial coordinates (x_s, y_s, z_s) , and initial pressure p_0 , we detail the parameters of its 10th-order spherical decomposition: The coordinates of the centers of the 10 spheres are all (x_s, y_s, z_s) , the radii of the spheres and the initial sound pressure uniformly distributed on each sphere are shown below:

$$\begin{aligned} \text{radii: } & (0.5a_0, 0.6a_0, 0.9a_0, 1.2a_0, 1.5a_0, 1.8a_0, 2.1a_0, 2.4a_0, 2.7a_0, 3.0a_0), \\ \text{pressure: } & \left(\frac{10}{55}p_0, \frac{9}{55}p_0, \frac{8}{55}p_0, \frac{7}{55}p_0, \frac{6}{55}p_0, \frac{5}{55}p_0, \frac{4}{55}p_0, \frac{3}{55}p_0, \frac{2}{55}p_0, \frac{1}{55}p_0 \right). \end{aligned} \quad (1)$$

It is worth noting that this decomposition method is not unique. The choice of the 10th-order balances model accuracy and computational complexity. Using higher-order spherical decomposition can further improve computational accuracy, but the computational load will increase linearly with the order.

Based on the general expression for the photoacoustic pressure in a non-viscous, infinitely large homogeneous medium [34]:

$$p(\vec{r}, t) = \frac{1}{4\pi v_s^2} \frac{\partial}{\partial t} \left(\frac{1}{v_s t} \int d\vec{r}' p_0(\vec{r}') \delta \left(t - \frac{|\vec{r} - \vec{r}'|}{v_s} \right) \right), \quad (2)$$

we can further derive the analytical expression for the propagation of acoustic pressure in a sphere excited by a Dirac pulse [34]:

$$p(R, t) = p_0 \frac{R - v_s t}{2R} (u(R - v_s t + a_0) - u(R - v_s t - a_0)), \quad (3)$$

where \vec{r} is the position vector of the observation point, \vec{r}' is the position vector of the sphere's center, t is the propagation time, p_0 is the initial acoustic pressure of the sphere at time zero, a_0 is the radius of the sphere, R is the Euclidean distance between the observation point and the center of the sphere (thus $R > a_0$), and the unit step function $u(x)$ is given by:

$$u(x) = \begin{cases} 0, & x < 0 \\ 1, & x \geq 0 \end{cases}. \quad (4)$$

Based on the analytical expression for the propagation of acoustic pressure in a sphere excited by a Dirac pulse, we can derive the 10th-order spherical acoustic pressure propagation expression $P_{10\text{ball}}$. Furthermore, for a point source with resolution a_0 , spatial coordinates (x_s, y_s, z_s) , and initial acoustic pressure p_0 , the acoustic pressure propagation expression is given by $P = k \cdot P_{10\text{ball}}$, where $k = 1/14.35$ if the number of point sources exceeds 20, and $k = 1$ if the number of point sources is less than 20. The received acoustic pressure signal at any spatial location is obtained by the linear superposition of the acoustic pressure propagation expressions from all point sources. It is important to note that the value of k does not affect the reconstruction of our method, but is only required for the forward process of the probe data based on the sound source.

Due to the presence of the unit step function $u(x)$, the 10th-order spherical decomposition cannot be truly differentiable. To address this, we use the following high-precision formula to approximate the unit step function $u(x)$:

$$u_\epsilon(x) = \frac{1}{2}(1 + \text{erf}(1 + \epsilon x)), \quad (5)$$

$$\text{where } \text{erf}(x) = \frac{2}{\sqrt{\pi}} \int_0^x e^{-t^2} dt.$$

Considering the typical resolution of photoacoustic imaging, which ranges from 100 μm to 1 mm, we set the smoothness factor ϵ to 10^6 to ensure convergence to the unit step function.

Thus, we obtain the acoustic pressure propagation expression for a point source with resolution a_0 , spatial coordinates (x_s, y_s, z_s) , and initial acoustic pressure p_0 based on the 10th-order spherical decomposition:

$$p(R, t) = \sum_{i=1}^{10} p_0^i \frac{D}{2R} (u_\epsilon(D + a_0^i) - u_\epsilon(D - a_0^i)), \quad (6)$$

where a_0^i and p_0^i are the radius and initial pressure of the i th-order sphere in Eq. 1, and $D = R - v_s t$. In each step of the calculation it is fully differentiable.

(ii) Backward Propagation. After representing our forward prediction using a smooth step function, our forward prediction function $p(R, t)$ becomes fully differentiable. For the step function $u(x)$, its theoretical derivative is the impulse function $\delta(x)$; for our smooth step function, we have:

$$\delta_\epsilon(x) = \frac{d}{dx} u_\epsilon(x) = \frac{\epsilon}{\sqrt{\pi}} \exp(-\epsilon^2 x^2), \quad (7)$$

which is also a good approximation of the impulse function.

Thus, in the end-to-end training process, we need to compute the derivatives of $p(R, t)$ with respect to the initial pressure p_0 , the sphere radius a_0 , the sphere center coordinates (x_s, y_s, z_s) and the sensor coordinates (x_r, y_r, z_r) to propagate the gradient backward. Given that in Eq. 3, as we have:

$$R = \sqrt{(x_r - x_s)^2 + (y_r - y_s)^2 + (z_r - z_s)^2}, \quad (8)$$

$$D = R - v_s t,$$

we can derive:

$$\frac{\partial p}{\partial p_0} = \sum_{i=1}^{10} \frac{p_0^i}{p_0} \frac{D}{2R} (u_\epsilon(D + a_0^i) - u_\epsilon(D - a_0^i)),$$

$$\frac{\partial p}{\partial a_0} = \sum_{i=1}^{10} \frac{a_0^i}{a_0} p_0^i \frac{D}{2R} (\delta_\epsilon(D + a_0^i) + \delta_\epsilon(D - a_0^i)), \quad (9)$$

$$\begin{aligned} \frac{\partial p}{\partial x_s} &= \left(\frac{\partial p}{\partial R} + \frac{\partial p}{\partial D} \frac{\partial D}{\partial R} \right) \frac{\partial R}{\partial x_s} \\ &= -\frac{x_r - x_s}{R} \sum_{i=1}^{10} p_0^i \left(\frac{v_s t}{2R^2} (u_\epsilon(D + a_0^i) - u_\epsilon(D - a_0^i)) + \frac{D}{2R} (\delta_\epsilon(D + a_0^i) - \delta_\epsilon(D - a_0^i)) \right). \end{aligned}$$

The derivatives with respect to y_s and z_s are similar to the derivative with respect to x_s shown above. The above expression demonstrates the back-propagation computation of our differentiable rapid radiator. Both forward and backward model are implemented with GPU-accelerated code based on Taichi [35] and pure CUDA syntax.

3.2 Sliding Ball Adaptive Growth Variable-Resolution Point Cloud Model

In our point cloud representation, each point represents a small sphere at a specific resolution with five attributes: x, y, z, a_0, p_0 . Here, x, y, z are the spatial coordinates of the point, a_0 is the resolution information carried by the point (i.e., the "radius of the sphere"), and p_0 is the initial acoustic pressure of the point. All of these attributes can be subject to gradient computations.

The overview framework of Sliding Ball Adaptive Growth algorithm is given in Fig. 1(a). We begin by randomly initializing the point cloud within the spatial range that requires reconstruction. This randomly initialized point cloud

serves as the acoustic source. Using our differentiable rapid radiator, the acoustic signals received at the sensor locations can be simulated. By calculating the loss between these simulated signals and the actual sensor data and performing gradient back-propagation, the model can update all attributes of the points in the point cloud. All the optimization methods of each point in the point cloud are demonstrated in Fig. 1(c).

It is important to emphasize that, despite the capability of our differentiable rapid radiator to compute the gradient of the loss with respect to the spatial coordinates, resolution, and initial acoustic pressure, our model restricts updates to only the resolution and initial acoustic pressure during the coarse reconstruction stage. The spatial coordinates of the points remain unchanged at this stage, and the model’s duplication feature is not activated.

Algorithm 1 SlingBAG

Input: Z_0 : Randomly initialized point cloud
 S_0 : Real signal
 (x, y, z, a_0, p_0) : Attributes of each point

Output: 3D reconstruction result in form of voxel grid

- 1: Coarse reconstruction stage:
- 2: **while not converged do**
- 3: Generate signal S_1 by forward simulation with differentiable rapid radiator
- 4: Calculate loss: $L = \|S_1 - S_0\|_2$
- 5: Gradient back-propagation through differentiable rapid radiator: $\frac{\partial L}{\partial a_0}, \frac{\partial L}{\partial p_0}$
- 6: Update on (a_0, p_0)
- 7: Splitting and destroying of points in Z_0
- 8: **end while**
- 9: Coarse 3D reconstruction result Z_1 in form of point cloud
- 10:
- 11: Fine reconstruction stage:
- 12: **while not converged do**
- 13: Generate signal S_2 by forward simulation with differentiable rapid radiator
- 14: Calculate loss: $L = \|S_2 - S_0\|_2$
- 15: Gradient back-propagation through differentiable rapid radiator: $\frac{\partial L}{\partial x}, \frac{\partial L}{\partial y}, \frac{\partial L}{\partial z}, \frac{\partial L}{\partial a_0}, \frac{\partial L}{\partial p_0}$
- 16: Update on (x, y, z, a_0, p_0)
- 17: Duplicating, splitting and destroying of points in Z_1
- 18: **end while**
- 19: Fine 3D reconstruction result Z_2 in form of point cloud
- 20:
- 21: **for each point in Z_2 do**
- 22: Convert into voxel grid through point cloud-voxel grid shader
- 23: **end for**

By focusing on updating the resolution and initial acoustic pressure during the early stages, the model can achieve rapid convergence while maintaining computational efficiency. This adaptive approach allows for precise control over the model’s refinement process, ultimately leading to high-quality 3D photoacoustic reconstructions even with sparsely distributed sensors.

Then, after a certain number of iterations, the model undergoes adaptive density optimization of the point cloud to ensure computational efficiency and prevent convergence to sub-optimal solutions that violate physical principles. Points with excessively low initial acoustic pressure or resolution values are discarded to maximize resource savings and expedite iteration speed. For points with excessively large resolution values, the model performs a splitting operation. This involves splitting an initially large-radius sphere into two smaller-radius spheres, each with half the original radius, while maintaining the same initial acoustic pressure. The splitting direction can be aligned with the gradient direction of the point position.

As the loss begins to converge, the model further enhances its capabilities by incorporating position coordinate updates into the optimizer alongside updates for initial acoustic pressure and radius, and the point cloud enters into fine reconstruction stage. The model then activates its duplication feature at specific iteration counts, enabling all points in the current point cloud to be duplicated along their respective position gradients. This approach increases the point cloud’s density and allows for more precise control and fine-tuning of each point, leading to more detailed and accurate 3D reconstructions.

Through these processes, the model can further refine the point cloud, improving the resolution and detail of the 3D reconstruction. This adaptive and iterative approach facilitates high-quality 3D photoacoustic imaging reconstructions even under conditions of extremely sparse sensor distributions.

3.3 Physically-Based Point Cloud to Voxel Grid Shader

While the 3D point cloud, resulting from iterative processing, encapsulates all the information about the reconstructed acoustic sources, directly visualizing the point cloud doesn't convey each point's resolution and initial acoustic pressure effectively. Voxel grids are extensively used in the photoacoustic imaging field for 3D visualization, leading us to develop a converter, termed the "Point Cloud to Voxel Grid Shader," which converts point cloud data into voxel grid information.

Due to the density of the point cloud, its coordinates will not be perfectly aligned with the voxel grid nodes. The shader first aligns the voxel grid coordinate space with the point cloud coordinate space in three dimensions. Next, the shader iterates over all the points in the point cloud and reads each point's initial acoustic pressure and resolution information corresponding to the gray-scale intensity and brush size, respectively. These attributes are then refined via the decomposition coefficients from the 10th-order spherical decomposition used in the differentiable rapid radiator.

Here's a detailed breakdown of the conversion process:

1. **Alignment of Coordinate Spaces:** The voxel grid coordinate space and the point cloud coordinate space are aligned in 3D space to ensure accurate correspondence.
2. **Reading Point Attributes:** For each point in the point cloud, the shader reads the initial acoustic pressure and resolution information. These attributes, representing gray-scale intensity and brush size, are adjusted based on the coefficients from the 10th-order spherical decomposition.
3. **Voxel Grid Coloring:** The shader "paints" each point into the 3D space, using the adjusted gray-scale intensity and brush size. The markings interact with the voxel grid, mapping the gray-scale intensity onto the grid nodes. The voxel grid nodes' intensity values are accumulated when multiple brushstrokes overlap, ensuring a complete rendering of the voxel grid from the point cloud data.

By converting point cloud data into a voxel grid using this physically-based point cloud to voxel grid shader, comprehensive and detailed 3D visualization is achieved, accurately reflecting the initial acoustic pressures and resolutions from the original point cloud data. This method leverages the strengths of both point cloud and voxel grid representations, facilitating enhanced visualization for analysis and interpretation in the field of photoacoustic imaging.

4 Results

Point Cloud Dataset:

Based on previous work on the 3D imaging of peripheral arm vessels, we extracted numerical data from voxel grids at a resolution of 0.2 mm to create a relatively clean point cloud dataset of the hand peripheral vessels. This dataset was used as the simulated acoustic source to validate our reconstruction method. At a 0.2 mm resolution, the voxel grid size was $400 \times 520 \times 200$. Using the k-Wave simulation toolkit, we obtained the simulated signal data from the planar sensor array as the ground truth sensor signal.

4.1 Comparison of Forward Simulation Results: Differentiable Rapid Radiator vs. k-Wave

We first validated the accuracy of the forward simulation of the differentiable rapid radiator. We uniformly placed 200,000 sensors within an $80 \text{ mm} \times 100 \text{ mm}$ plane, positioned approximately 15 mm above the acoustic source ($75 \text{ mm} \times 0.2 \text{ mm}$ spacing), with a sampling rate set to 40 MHz and a sampling point count of 4096. Subsequently, we simulated the propagation of photoacoustic signals using both our differentiable rapid radiator and k-Wave. Fig. 2 illustrates the comparison of simulated signals at a specific sensor position obtained by the two methods. We then calculated the L_2 loss between the temporal signals obtained from both methods, and reshaped the (1, 4096) temporal signals into (64, 64) images to compute the SSIM between them. The results indicated that for the 200,000 sensors, the average SSIM of the simulated signals from both methods reached 99.51%, and the average L_2 loss was less than 0.00185. This indicates that our forward simulation of our differentiable rapid radiator has extremely high accuracy, capable of producing simulation results almost identical to those obtained with k-Wave at any distance scale.

It is noteworthy that while our method produced simulation results nearly identical to those of k-Wave, our simulation speed was significantly faster. We tested the simulation time for a single sensor. The results indicate that, in a

homogeneous, non-viscous medium with 60,000 sources, a resolution of 0.2 mm, a sampling rate of 40 MHz, and 4096 sampling points, for a single sensor, the k-Wave simulation time was 50,904 seconds, while the forward simulation time for the differentiable rapid radiator was 2.80 seconds, achieving a speedup of 18,180 times. Meanwhile, our differentiable rapid radiator only utilizes 0.32 GB of GPU memory, whereas k-Wave requires as much as 46.7 GB of GPU memory at this point, exceeding the single-card memory capacity limit of most GPUs.

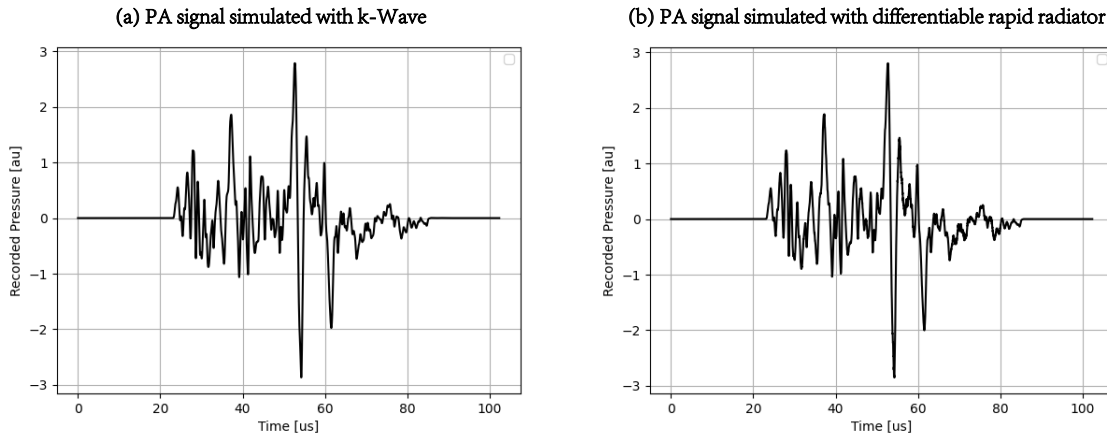


Figure 2: Comparison of forward simulation results between k-Wave and our differentiable rapid radiator. (a) Simulated signals obtained using k-Wave. (b) Simulated signals obtained using the differentiable rapid radiator.

4.2 High-Quality 3D Photoacoustic Reconstruction under Extremely Sparse Planar Array

We uniformly placed 200,000 sensors (with a spacing of 0.2 mm) within an $80 \text{ mm} \times 100 \text{ mm}$ plane situated approximately 15 mm ($75 \text{ mm} \times 0.2 \text{ mm}$) directly above the acoustic source to simulate the signal. Subsequently, to simulate an extremely sparse planar array, we extracted the coordinates and corresponding simulated signals from 238 sensors spaced 6 mm apart.

We first present the 3D reconstruction results displayed as heatmaps in Fig. 3. The SlingBAG reconstruction results have undergone both point cloud iteration and the conversion from point cloud to voxel grid. It should be mentioned that Fig. 3(d) is the SlingBAG reconstruction result with 8000 sensors spaced 1 mm apart extracted from total 200,000 sensors.

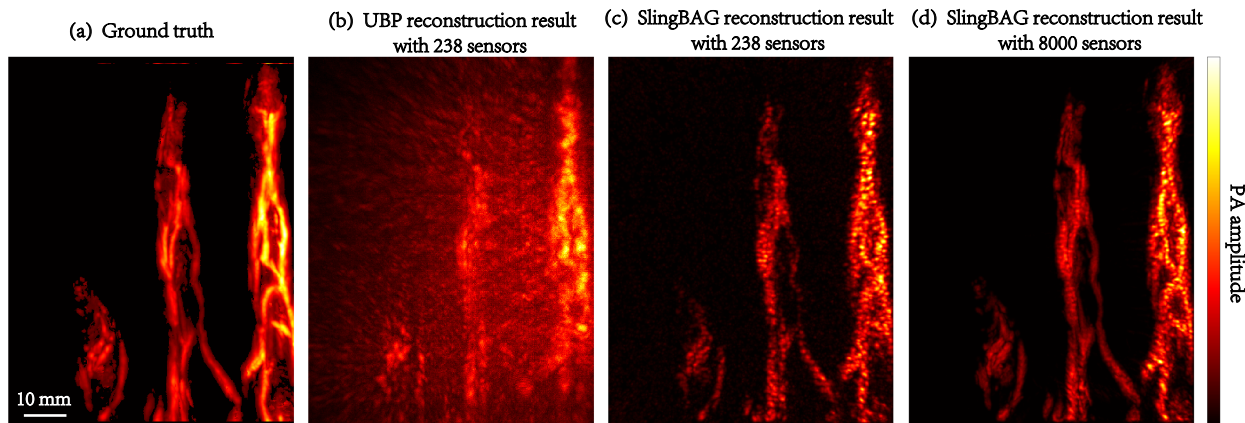
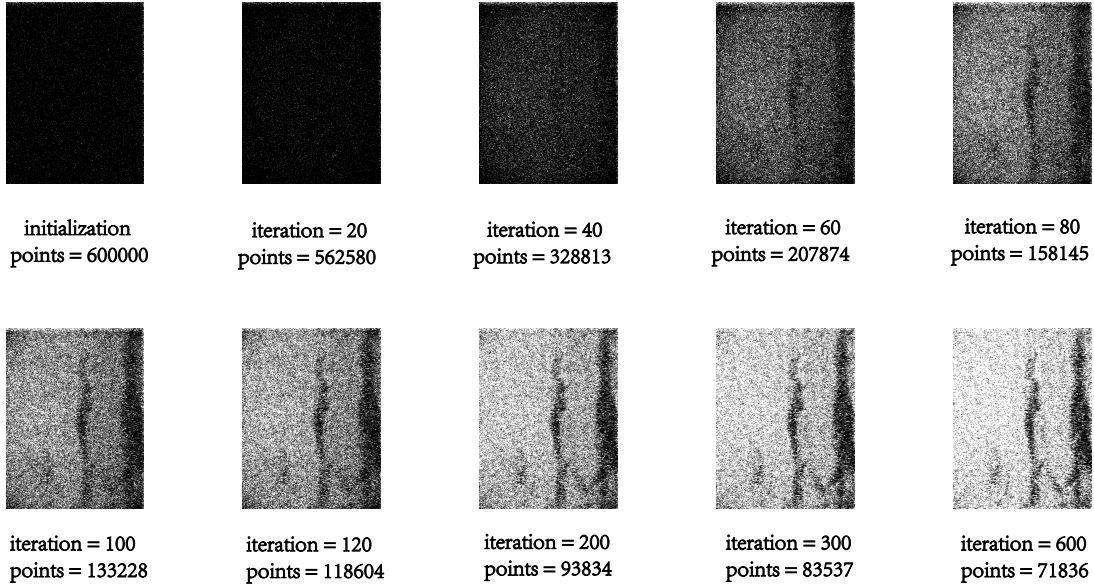
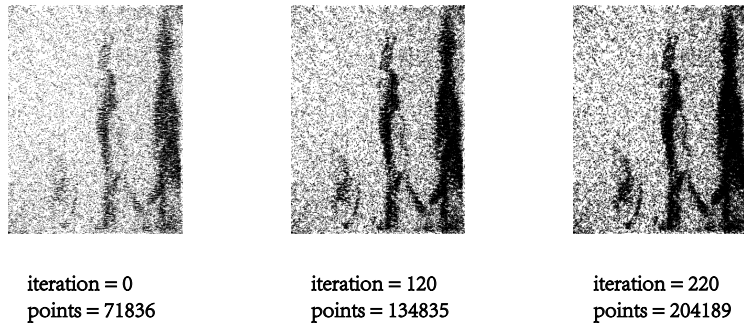


Figure 3: Comparison of 3D photoacoustic reconstruction results under extremely sparse sensor distribution. (a) Maximum amplitude projection of the acoustic source. (b) Maximum amplitude projection of the UBP reconstruction result with 238 sensors. (c) Maximum amplitude projection of the SlingBAG reconstruction result with 238 sensors. (d) Maximum amplitude projection of the SlingBAG reconstruction result with 8000 sensors. (Colorbar: hot. Scale: 10 mm.)

(a) Coarse reconstruction



(b) Fine reconstruction



(c) Reconstruction results of different stages

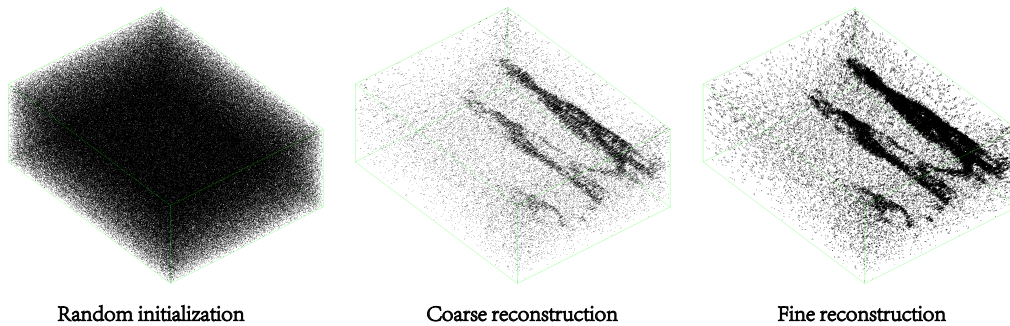


Figure 4: Point cloud optimization visualization results. (a) 3D visualization of point clouds at different iterations at the coarse reconstruction stage. (b) 3D visualization of point clouds at different iterations at the fine reconstruction stage. (c) 3D visualization of point clouds at various stages of the entire reconstruction process, including random initialization, coarse reconstruction stage, and fine reconstruction stage.

We visualized the iterative results of our reconstruction algorithm’s point cloud in Fig. 4. At coarse reconstruction stage, we initialized a relatively dense point cloud distribution randomly within the reconstruction area. During this stage, the position update and point cloud duplication features of the sliding ball adaptive growth variable resolution point cloud model were fixed. As shown in Fig. 4(a), with updates in the initial acoustic pressure and resolution of each point, as well as the implementation of the adaptive density optimization strategy, the densely initialized random point cloud gradually becomes sparser, ultimately converging to the shape of three finger vessels. Since the positions of the points are not updated at this stage, the coarse reconstruction stage yields only an initial convergence result.

Next, we enabled the model’s position update and point cloud duplication features. Fig. 4(b) displays the optimization process during the fine reconstruction stage. It can be seen that the converged shape of the three finger vessels obtained from the coarse reconstruction gradually becomes denser, with finer details such as small vessels becoming clearer and more continuous. Meanwhile, the L_2 loss, which initially converged to 4.21 during the coarse reconstruction phase, continues to decline and ultimately settles at 0.32.

Fig. 4(c) shows the 3D visualization results of the point cloud throughout the entire reconstruction process, from random initialization to coarse reconstruction result and finally to fine reconstruction result. The point cloud evolves from a dense random distribution into a sparse vessel structure, and ultimately becomes a dense and continuous vessel shape, completing the reconstruction from sparse sensor data to a dense 3D point cloud.

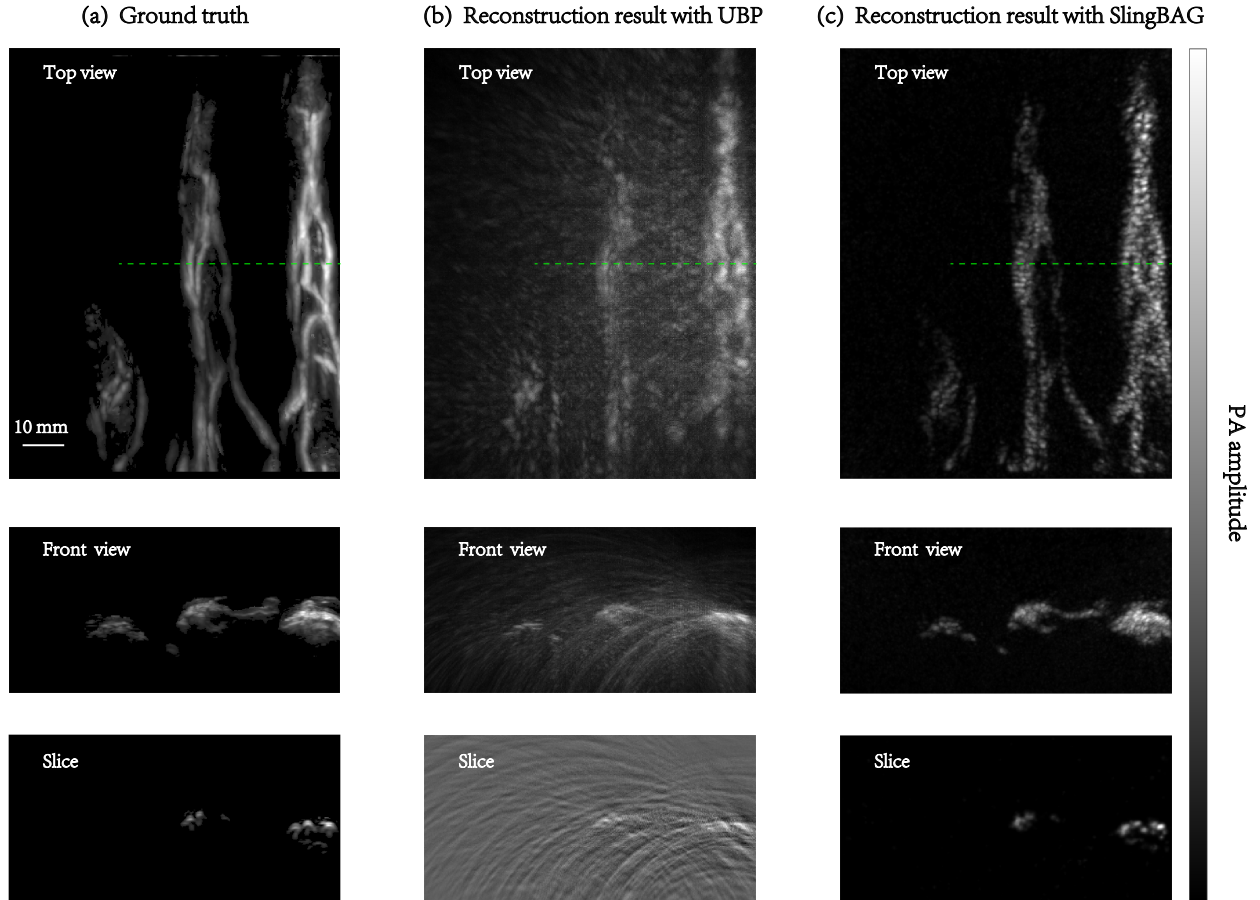


Figure 5: Comparison of 3D photoacoustic reconstruction results under extremely sparse planar arrays. (a) Top-view maximum amplitude projection, front-view maximum amplitude projection, and slice at the green dashed line in the top-view MAP of the acoustic source. (b) Top-view maximum amplitude projection, front-view maximum amplitude projection, and slice at the green dashed line in the top-view MAP of the UBP 3D reconstruction result. (c) Top-view maximum amplitude projection, front-view maximum amplitude projection, and slice at the green dashed line in the top-view MAP of the SlingBAG 3D reconstruction result. (Scale: 10 mm.)

Since each point in the point cloud contains information on position, resolution, and initial acoustic pressure, and because the point cloud representation cannot visualize resolution and initial acoustic pressure directly, we need to

project the detailed 3D point cloud reconstruction results onto a single-resolution voxel grid through a point cloud-to-voxel grid shader. In Fig. 5, we present the voxel grid results, which have a size of $400 \times 520 \times 200$ and a grid resolution of 0.2 mm.

Fig. 5 shows the comparisons of the ground truth, UBP reconstruction result, and SlingBAG reconstruction result, including top-view maximum amplitude projections, front-view maximum amplitude projections, and slices at the green dashed line position in the top-view maximum amplitude projection. It can be observed that with UBP reconstruction due to the very sparse distribution of sensors, the 3D reconstruction results exhibit strong reconstruction artifacts, and the signal strength of these artifacts is almost on the same order as the vascular signals, resulting in an SNR of 19.5 dB.

In contrast, the result reconstructed using SlingBAG clearly reveals the blood vessel structures with much less reconstruction artifacts and an SNR reaching 41.3 dB.

4.3 Quantitative Validation: Synthesizing New Sensor Data Using 3D Reconstruction Results

To validate the quantitative accuracy of the reconstruction results obtained using the SlingBAG algorithm, we used the 3D vessels result in subsection 4.2 reconstructed from the data of 238 sensors with SlingBAG algorithm as the acoustic source. We then simulated the signals at other sensor positions among 200,000 possible positions, excluding the 238 sensors used for the reconstruction. Comparing the simulation results of the 3D blood vessels reconstructed from sparse sensor data with the simulation results of the true 3D blood vessels, we found that the average L_2 loss between the two was approximately 0.15, and the average SSIM exceeded 80% (see in Fig. 6). This indicates that the 3D photoacoustic imaging results reconstructed using the SlingBAG algorithm can be reliably used to generate temporal signals for sensors at new positions. This shows great potential of our SlingBAG algorithm for research in photoacoustic imaging sensor interpolation.

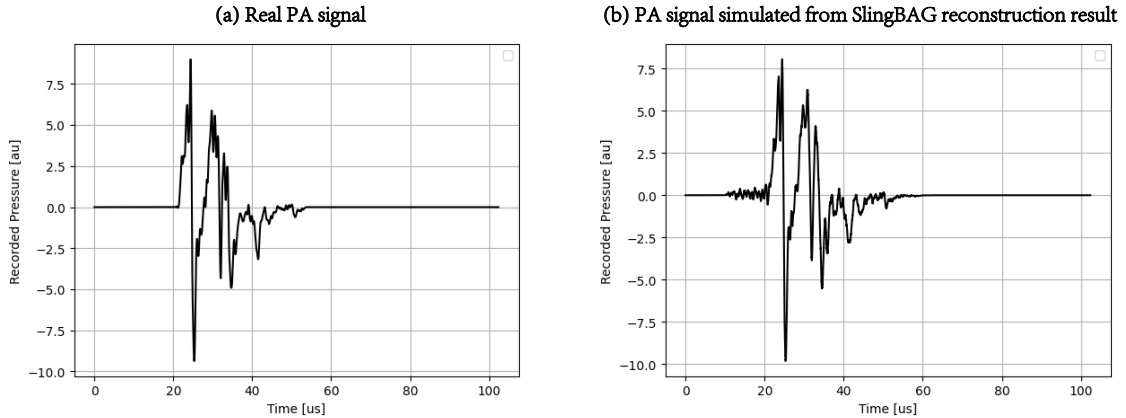


Figure 6: Comparison of real PA signal and PA signal simulated from SlingBAG reconstruction result. (a) New PA signals at different positions obtained through simulations based on the real acoustic source. (b) New PA signals at different positions obtained through simulations based on the 3D reconstruction result using the SlingBAG algorithm with 238 sensors' signals.

4.4 Image Reconstruction under Sparse Sensor Distribution with Noise

To validate the robustness of the SlingBAG reconstruction algorithm, we added Gaussian white noise at levels of 2.5% and 10% to the simulated signals used for reconstruction. The temporal signals from the sensors after noise addition are shown in Fig. 7.

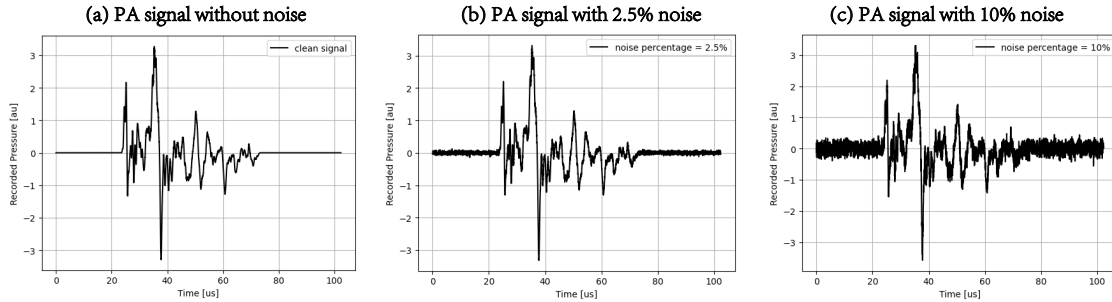


Figure 7: PA signals with different levels of Gaussian noise. (a) Simulated signals without added noise. (b) Simulated signals with 2.5% Gaussian white noise. (c) Simulated signals with 10% Gaussian white noise.

The reconstruction results using the SlingBAG algorithm are shown in Fig. 8. It can be observed that as the noise level in the PA signals increases, the reconstruction results from the SlingBAG algorithm become progressively blurrier. Using the original acoustic source as a reference, we calculated the PSNR of the top-view maximum amplitude projection and the front-view maximum amplitude projection for the reconstruction results obtained from the 238 sensor signals without noise, with 2.5% added noise, and with 10% added noise.

The results indicate that the PSNR of the top-view maximum amplitude projection for the reconstructions without noise, with 2.5% noise, and with 10% noise are 22.54 dB, 22.26 dB and 21.67 dB, respectively. For the front-view maximum amplitude projection, the PSNR values are 27.53 dB, 27.37 dB and 27.01 dB, respectively.

These findings reveal that as the noise proportion in the signals increases, the quality of the reconstruction results from the SlingBAG algorithm slightly decreases, while it still remains within the same order of magnitude. This demonstrates the resistance of the SlingBAG algorithm to noise.

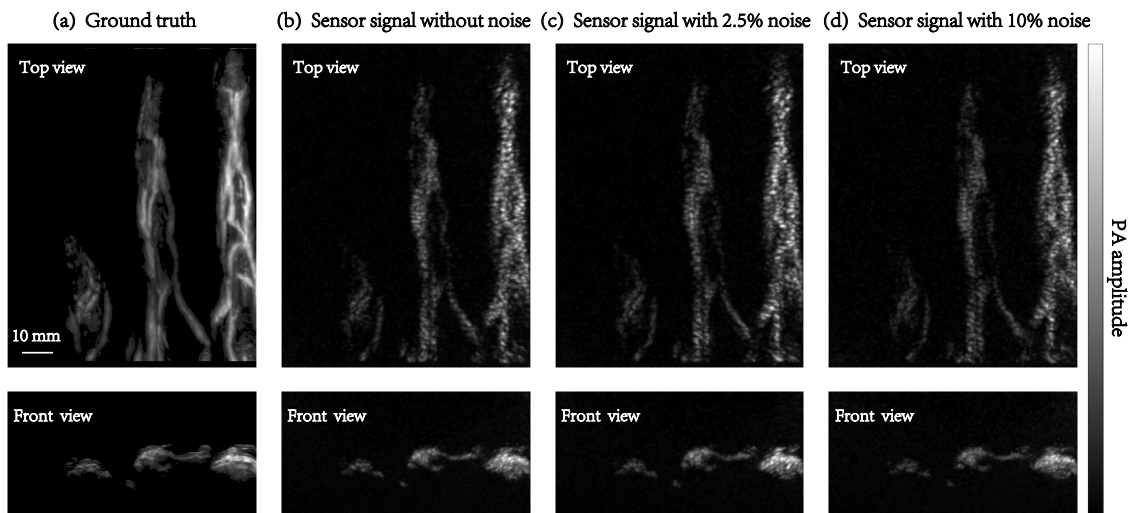


Figure 8: The reconstruction results of the SlingBAG algorithm with different levels of Gaussian noise added to the sensor signals. (a) Top-view-MAP and front-view-MAP of the real acoustic source. (b) Top-view-MAP and front-view-MAP of the 3D reconstruction result obtained without added signal noise. (c) Top-view-MAP and front-view-MAP of the 3D reconstruction result obtained with 2.5% Gaussian white noise added to the signal. (d) Top-view-MAP and front-view-MAP of the 3D reconstruction result obtained with 10% Gaussian white noise added to the signal. (Scale: 10 mm.)

4.5 Validation of Quantitative Imaging Results

In this subsection, we quantitatively evaluate the numerical accuracy of the 3D images reconstructed by the SlingBAG algorithm.

We further increased the density of the sensor arrangement, sampling sensors at intervals of 2mm, thereby extracting 2000 sensors from the pool of 200,000 sensors. The 3D reconstruction result with 2000 sensors is shown in Fig. 9. We calculated the SSIM between the reconstruction result and the 3D source volume, achieving an SSIM of 0.9746. In comparison, the SSIM between the reconstruction result from 238 sensors and the 3D source volume was 0.9562. These findings indicate that our reconstruction results exhibit high accuracy in terms of 3D volumetric data, with precise localization of the acoustic source. As the sensor number increased from 238 to 2000 and the sensor interval distance decreased from 6 mm to 2 mm, the SSIM between the reconstructed 3D volume and the source improved by 1.84%. Additionally, denser sensor arrangements yielded more continuous and detailed reconstruction results. As highlighted by the red arrows in Fig. 9, the reconstruction result from 238 sensors appears more discrete and exhibits certain shape distortions compared to ground truth, whereas the result from 2000 sensors shows a significantly more continuous segment of the blood vessel, closely matching the original source.

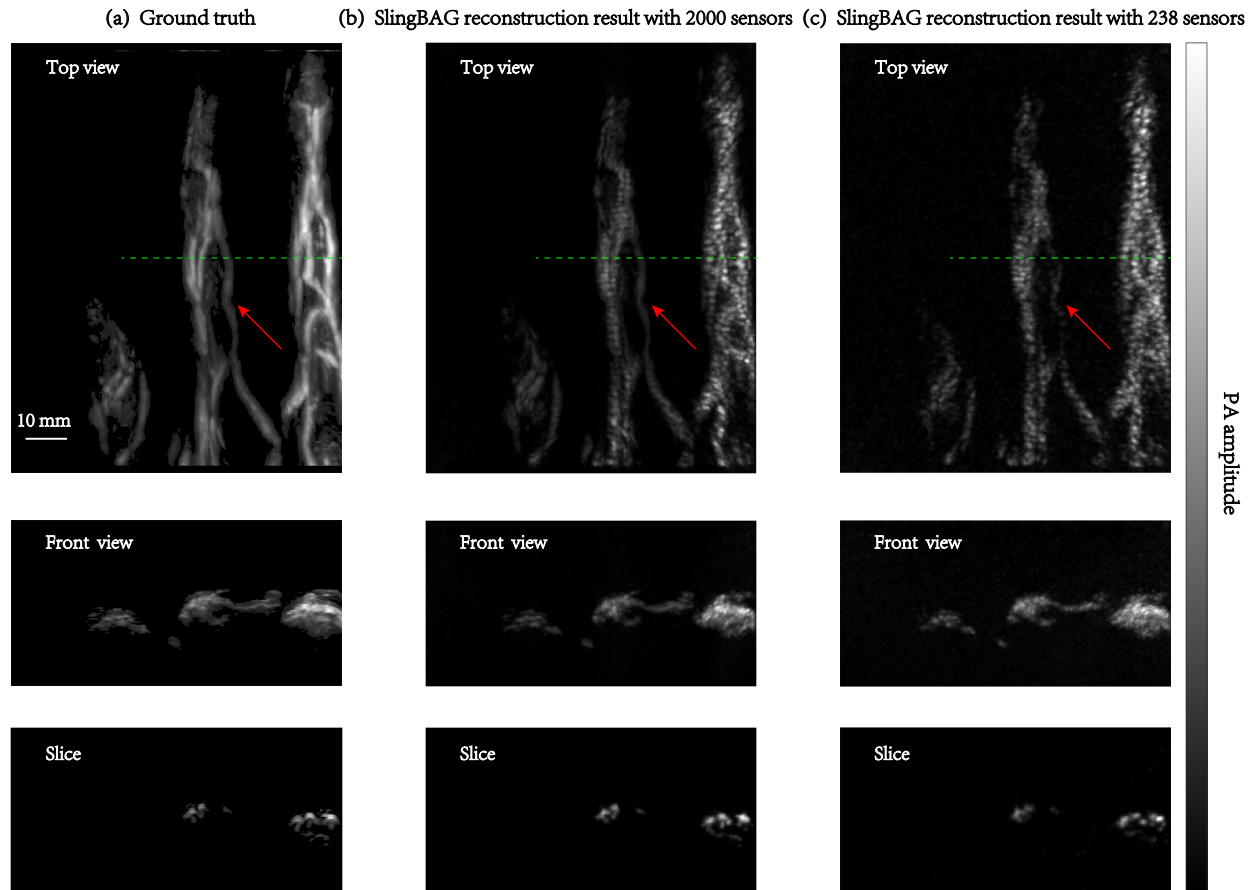


Figure 9: Comparison of SlingBAG 3D reconstruction results with 238 sensors and 2000 sensors. (a) Top-view-MAP, front-view-MAP, and slice at the green dashed line in the top-view-MAP of the acoustic source. (b) Top-view-MAP, front-view-MAP, and slice at the green dashed line in the top-view-MAP of the 3D reconstruction result obtained using the SlingBAG algorithm with 238 sensor signals. (c) Top-view-MAP, front-view-MAP, and slice at the green dashed line in the top-view-MAP of the 3D reconstruction result obtained using the SlingBAG algorithm with 2000 sensor signals. (Scale: 10 mm.)

We also introduced more stringent quantitative metrics, including the top-view maximum amplitude projection SSIM, front-view maximum amplitude projection SSIM, and the 3D SSIM for the non-zero signal volume. The top-view maximum amplitude projection SSIM computes the SSIM between the top-view maximum amplitude projections of the reconstruction and the source. Similarly, the front-view maximum amplitude projection SSIM calculates the SSIM between the front-view maximum amplitude projections of the reconstruction and the source. The non-zero signal 3D SSIM, which we pioneered as a rigorous standard for evaluating quantitative accuracy, excludes voxels that are zero in both the reconstructed and source voxel grids from the SSIM calculation, focusing solely on the remaining voxels. The

SSIM maps of the top-view maximum amplitude projection and the front-view maximum amplitude projection are shown in Fig. 10.

The results show that for the reconstruction from 2000 sensors, the top-view maximum amplitude projection SSIM was 0.7025, the front-view maximum amplitude projection SSIM was 0.6296, and the non-zero signal 3D SSIM was 0.4633. In contrast, for the reconstruction from 238 sensors, the corresponding SSIM values were 0.3856 for the top-view maximum amplitude projection, 0.2534 for the front-view maximum amplitude projection, and 0.3608 for the non-zero signal 3D SSIM.

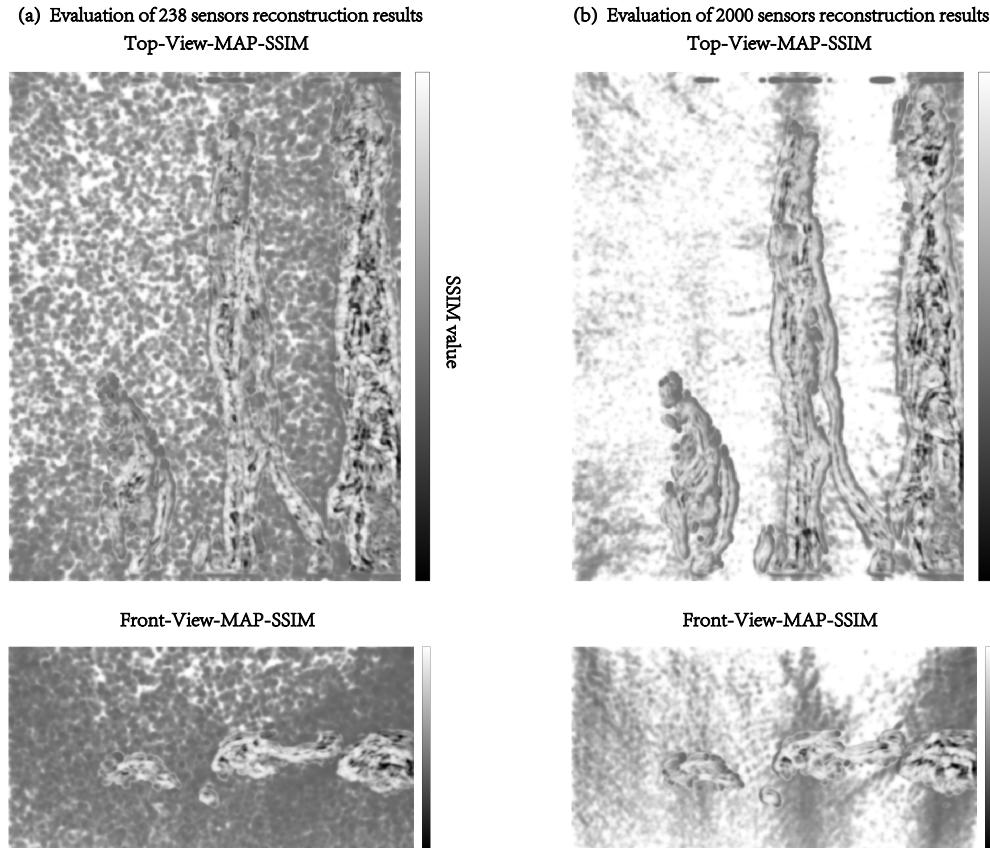


Figure 10: Evaluation of 3D reconstruction results with 238 sensors and 2000 sensors. (a) Top-view-MAP-SSIM between the reconstruction result using 238 sensor signals and the real acoustic source. (b) Top-view-MAP-SSIM between the reconstruction result using 2000 sensor signals and the real acoustic source.

Furthermore, we conducted a quantitative analysis of the slice images of the acoustic source, the reconstruction results from 2000 sensors, and the reconstruction results from 238 sensors. The SSIM between the slice of the reconstruction result from 2000 sensors and the slice of the acoustic source reached 97.4%, while the SSIM between the slice from 238 sensors and the acoustic source slice was 95.4%. In Fig. 11, we plotted the normalized signal intensity distribution along the yellow dashed line in the slice images for comparison (the dashed line's length does not represent the horizontal axis of the curve). In Fig. 11(d), the green solid line represents the intensity distribution of the acoustic source, the red dashed line represents the intensity distribution of the reconstruction result from 2000 sensors, and the blue dashed line represents the intensity distribution from 238 sensors. As the number of sensors increases from 238 to 2000, the intensity distribution along the yellow dashed line in the slice progressively approximates the true intensity distribution of the acoustic source. The discernibility of several "peaks" in the intensity distribution also significantly improves, indicating that the SlingBAG algorithm's reconstruction accuracy is strongly positively correlated with the density of sensor distribution. The intensity distribution for the 238-sensor reconstruction can only distinguish 3 "peaks", whereas the intensity distribution for the 2000-sensor reconstruction can accurately correspond to all five "peaks" in the source's intensity distribution.

Despite the fact that 2000 sensors still constitute a very sparse distribution for a region of $40 \text{ mm} \times 104 \text{ mm} \times 80 \text{ mm}$, resulting in minor deviations between the reconstructed intensity distribution and the true source intensity distribution, these deviations are limited to the peak magnitudes, with the peak positions being very accurate. As the number of sensors increases further, the reconstructed results will increasingly approximate the true acoustic source. Quantitative imaging results confirm that the SlingBAG algorithm not only has high localization precision for acoustic sources but also exhibits high numerical accuracy in reversing the initial acoustic pressure.

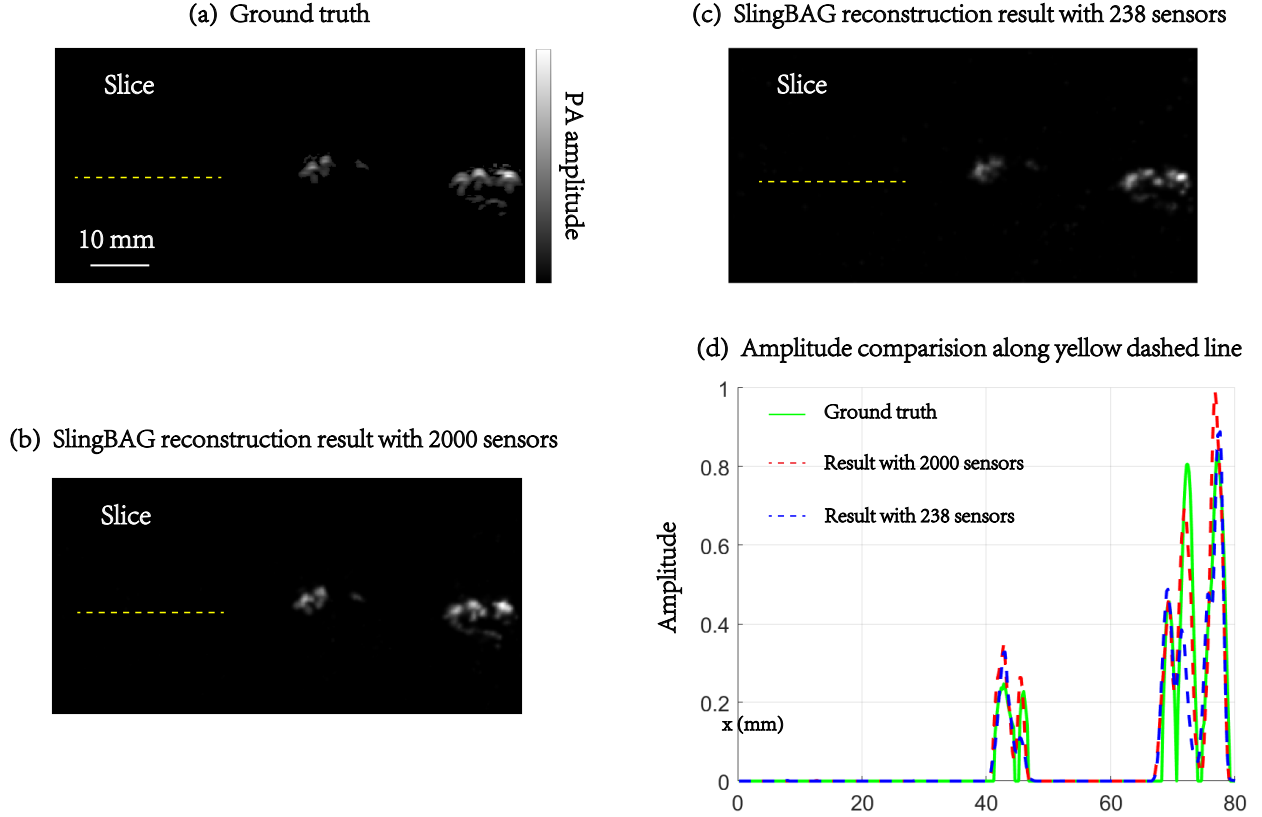


Figure 11: Comparison of slice results with 238 sensors and 2000 sensors. (a) Slice at the green dashed line in the top-view-MAP of the real acoustic source shown in Fig. 9. (b) Slice at the green dashed line in the top-view-MAP of the reconstruction result using 238 sensor signals shown in Fig. 9. (c) Slice at the green dashed line in the top-view-MAP of the reconstruction result using 2000 sensor signals shown in Fig. 9. (d) Intensity distribution curves along the yellow dashed line in the vertical coordinate of the slices from the real acoustic source, 238-sensor reconstruction, and 2000-sensor reconstruction. (Scale: 10 mm.)

4.6 SlingBAG reconstruction of in vivo mouse brain

In this subsection, we performed reconstructions using both the UBP and our SlingBAG algorithm based on real mouse brain data provided by Professor Chulhong Kim. During the reconstruction process, we investigated the reconstruction results under three different sampling strategies: reconstruction with all the 1024 elements, reconstruction under limited-view, and reconstruction under sparse-view. We visualized these sampling strategies in Fig. 12. For the limited-view reconstruction, we utilized signal data from only the top 512 elements of the hemisphere and from only the bottom 512 elements of the hemisphere. For the sparse-view reconstruction, we performed downsampling along the hemispherical azimuthal direction on the 1024 elements, extracting signal data from 512 elements for reconstruction. The mouse brain data was acquired by researchers in Kim’s lab using a 1024-element hemispherical US transducer array [36]. Each US transducer element in the array had an average center frequency of 2.02 MHz and a bandwidth of 54%. The effective field of view (FOV) was $12.8 \text{ mm} \times 12.8 \text{ mm} \times 12.8 \text{ mm}$ along the x, y, and z axes, respectively, and the spatial resolutions of approximately $380 \mu\text{m}$ were nearly isotropic in all directions when all 1024 US transducer elements were used [36]. More information regarding the hemispherical ultrasound array can be found in Kim’s publications [36, 37, 38, 39, 40].

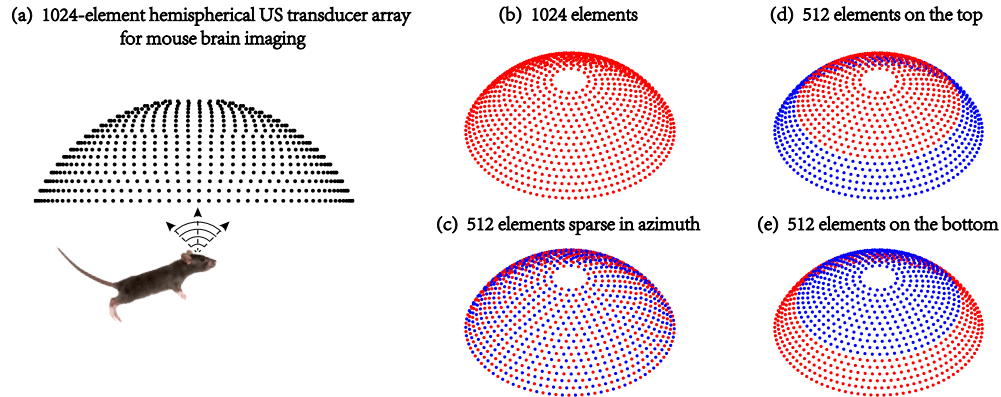


Figure 12: Mouse brain 3D photoacoustic reconstruction under limited-view and sparse-view. Red points indicates elements used in the reconstruction; blue points indicates elements not used. (a) Schematic diagram of the hemispherical array imaging the mouse brain. (b) 1024 elements. (c) Sparse-view 3D reconstruction where 512 elements are extracted by downsampling along the azimuthal direction. (d) Limited-view 3D reconstruction using only the top 512 elements of the hemisphere. (e) Limited-view 3D reconstruction using only the bottom 512 elements of the hemisphere.

We first compared the UBP results and SlingBAG reconstruction results reconstructed with all the 1024 elements in Fig. 13. We analyzed the signal-to-noise ratio (SNR) by examining specific slices along the green dashed line in Fig. 13. The SNR of the UBP reconstruction was 29.92 dB, whereas the SNR of the SlingBAG reconstruction reached 47.33 dB.

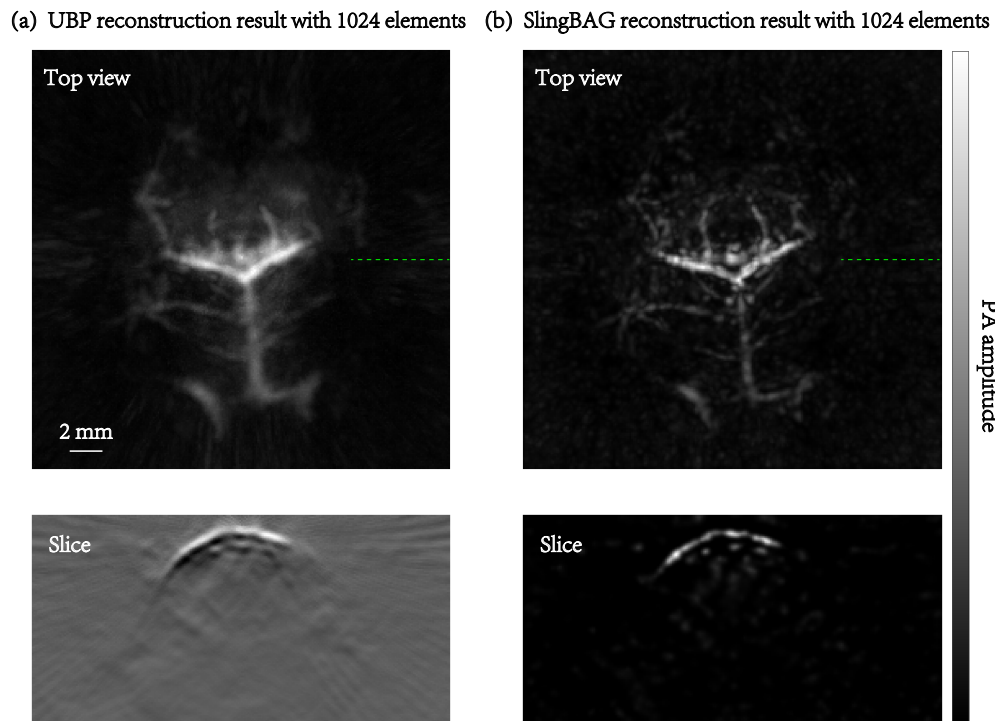


Figure 13: Comparison of mouse brain 3D PAI reconstruction. (a) Top-view maximum amplitude projection and slice at the green dashed line of the 3D reconstruction result using 1024 sensor signals with the UBP algorithm. (b) Top-view maximum amplitude projection and slice at the green dashed line of the 3D reconstruction result using 1024 sensor signals with the SlingBAG algorithm. (Scale: 2 mm.)

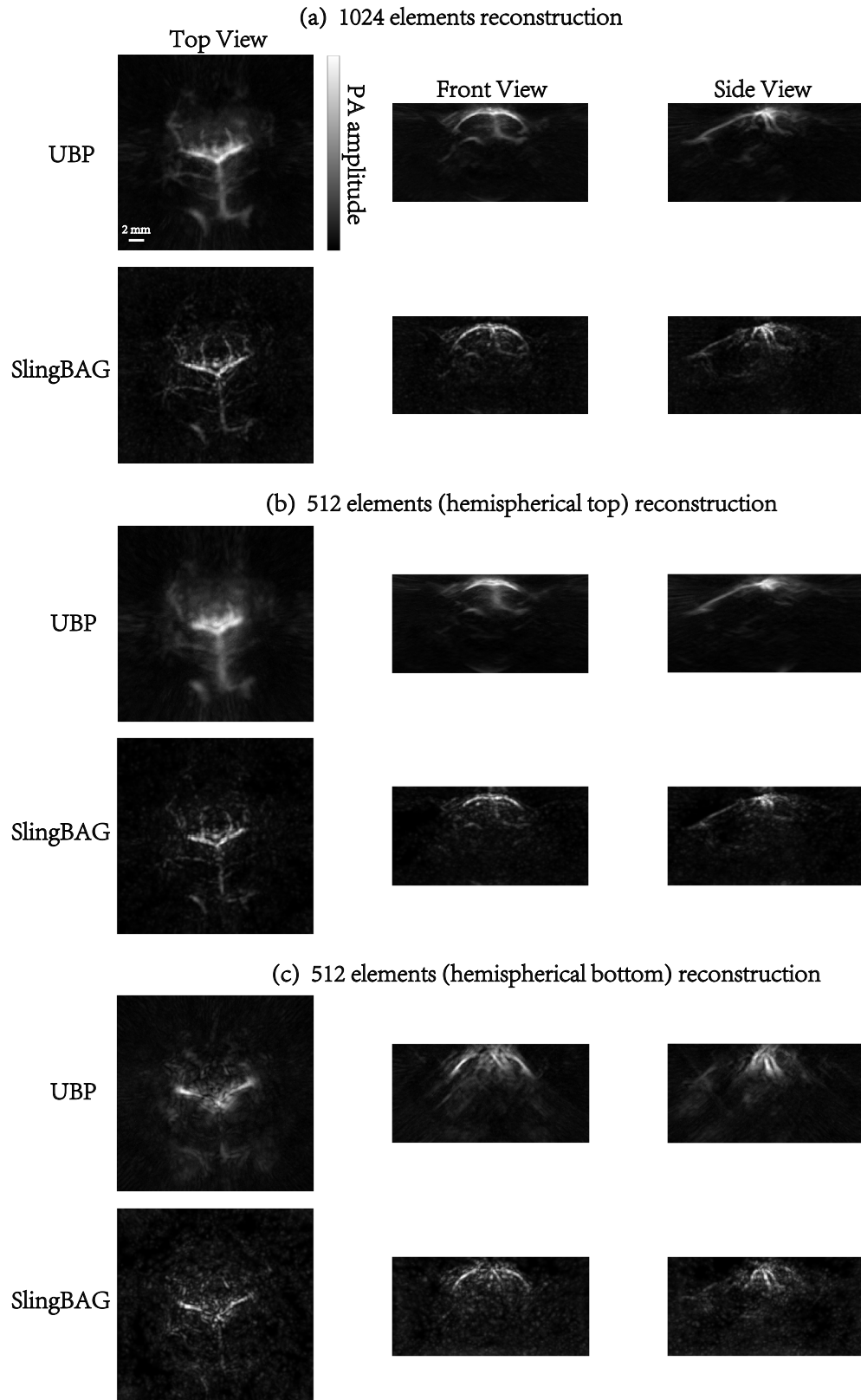


Figure 14: Top-view-MAP, front-view-MAP, and side-view-MAP of 3D reconstruction results of mouse brain under limited-view using: (a) 1024 sensor signals with UBP and SlingBAG algorithms. (b) Top 512 sensors of the hemisphere with UBP and SlingBAG algorithms. (c) Bottom 512 sensors of the hemisphere with UBP and SlingBAG algorithms. (Scale: 2 mm.)

Next, we investigated the impact of limited-view on the reconstruction performance of both UBP and SlingBAG. We conducted reconstructions using the top 512 sensors and the bottom 512 sensors of the hemisphere. The results are shown in Fig. 14. The reconstruction results indicate that SlingBAG has a significant advantage over UBP in terms of improving the SNR of the reconstruction results. However, when there is angular coverage loss in the sensor arrangement, both SlingBAG and UBP lose some vascular imaging information.

We further downsampled the 1024 sensors along the azimuthal angle, extracting 512 sensor positions and signals to perform 3D photoacoustic reconstruction. We compared the SlingBAG and UBP reconstruction results with those obtained using the full set of 1024 sensors to explore the impact of sparse distribution on the reconstruction performance of both methods. It can be observed in Fig. 15 that, under sparse sensor distribution conditions, SlingBAG achieves a higher SNR and fewer reconstruction artifacts compared to UBP. However, as the number of sensors decreased from 1024 to 512, the continuity of the blood vessels in the SlingBAG reconstruction results noticeably diminished, although it still managed to delineate the morphology of fine vessels.

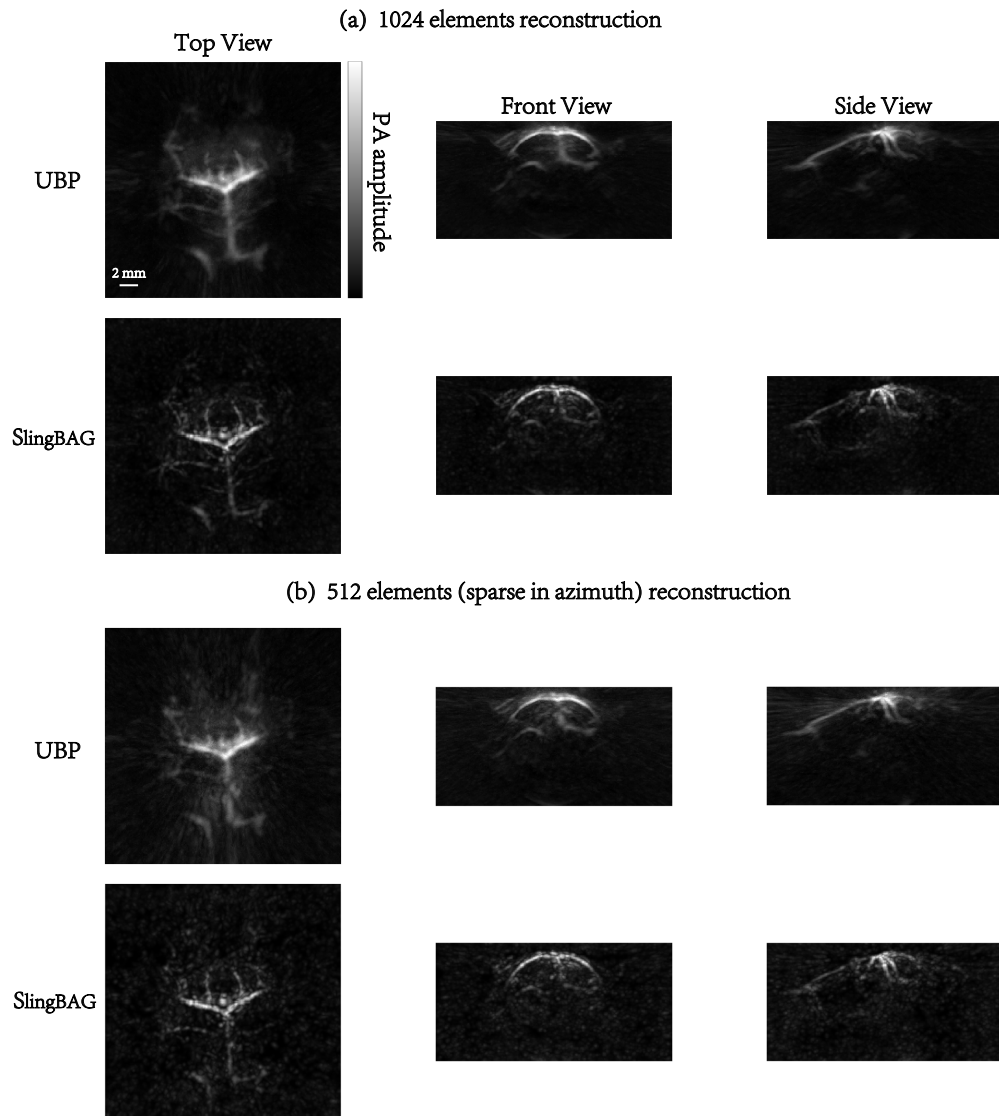


Figure 15: Top-view-MAP, front-view-MAP, and side-view-MAP of the 3D reconstruction results of mouse brain using: (a) 1024 sensor signals with the UBP and SlingBAG algorithms. (b) 512 sensors obtained by sparse sampling along the hemispherical azimuthal direction with the UBP and SlingBAG algorithms. (Scale: 2 mm.)

In summary, by comparing the reconstruction results of SlingBAG and UBP under conditions of sparse-view and limited-view, it is apparent that the SlingBAG reconstruction algorithm is better suited to handle sparse sensor distributions.

The SlingBAG algorithm significantly improves the quality of 3D reconstruction results in scenarios with sparsely distributed sensors, maintaining robust performance even with fewer sensing elements.

5 Discussion

Three-dimensional photoacoustic imaging (PAI) combines optical contrast with ultrasonic depth penetration, making it a highly promising modality for biomedical imaging. High-quality 3D photoacoustic reconstructions using sparsely distributed detectors have garnered significant attention. This paper proposes a point cloud iteration-based 3D photoacoustic imaging reconstruction algorithm, SlingBAG, which substantially increases speed with much less memory consumption. We have validated its effectiveness in achieving high-quality 3D reconstructions under extremely sparse sensor distributions using simulated hand vessel data and real mouse brain data. The SlingBAG algorithm provides substantially higher reconstruction quality than UBP with the same sensor photoacoustic signal data, effectively suppressing reconstruction artifacts.

Compared with traditional IR methods, our SlingBAG reconstruction method has two unique advantages: large reconstruction range with much less memory consumption and fast reconstruction speed with high reconstruction accuracy.

The simulated hand vessels data spans dimensions of $40 \text{ mm} \times 104 \text{ mm} \times 80 \text{ mm}$ in physical space. For traditional voxel grids, the same size of acoustic source distribution at a 0.2 mm resolution reaches grid sizes of $200 \times 520 \times 400$. When using signal data from 238 sensors for sparse reconstruction, each sensor has 4096 sampling points at a 40 MHz sampling frequency. This data volume is nearly impractical for traditional voxel-based iterative reconstruction methods in terms of memory usage and time consumption. However, our method requires only less than 3 GB of GPU memory. Regarding the widely used forward model k-Wave, its k-space pseudo-spectral method’s memory consumption heavily depends on the defined spatial grid size. This implies that in three-dimensional simulations, the memory usage will increase rapidly. Additionally, in iterative algorithms, this imposes a significant memory burden on gradient computation and optimizers, which is unacceptable for most integrated laboratory equipment and medical imaging systems.

Moreover, concerning computational time consumption, k-Wave requires computing the acoustic field at each time step, unlike our method, which directly calculates the far-field acoustic field for the forward model. This computational time cost limits its application in reconstruction algorithms for large-field-of-view 3D PACT imaging systems (where a large number of time steps are often required, such as the 4096 steps we use). For the mentioned spatial grid, 238 sensors, and 4096 time steps, using the same RTX 3090 Ti GPU, the forward process in our method takes only 18 seconds (because of the sparsity of the PACT imaging signal, where we only need to use a point cloud with 600,000 sources). In contrast, k-wave takes more than 1000 seconds, making it more than 55 times slower than our method.

In our method, the coarse reconstruction converges after 300 iterations, taking 9380 seconds, and the fine reconstruction converges after 220 iterations, taking 8400 seconds—altogether, less than 5 hours. The experiments were conducted on an RTX 3090 Ti GPU. The significant advantages in reconstruction range and speed are largely attributable to the point cloud representation, which inherently better aligns with the densely sampled regions and sparsely sampled areas typically found in genuine photoacoustic signal sources. Furthermore, the discrete nature of voxel grids is inherently incompatible with source density. Hence, considering physical model accuracy and computational cost, we believe that point cloud representation offers a better description of photoacoustic signal sources than voxel representation. Additionally, our differentiable rapid radiator ensures that both the forward simulation and the backward gradient propagation are fully differentiable, allowing for rapid parameter updates.

The SlingBAG reconstruction algorithm exhibits high precision. Comparing the reconstruction results with the simulated acoustic source demonstrates that the algorithm achieves excellent localization and numerical accuracy in reconstructing photoacoustic imaging sources. Whether evaluating on the quality of reconstructed images or the synthetic sensor data at new positions based on the reconstruction results, SlingBAG performs excellently. The high reconstruction accuracy is attributable to two factors: (1) Unlike voxel grid models, where the voxel resolution can limit spatial precision, point cloud models allow the source to converge to finer spatial locations; (2) The high accuracy of the forward simulation used in the differentiable rapid radiator of the SlingBAG algorithm, which accurately describes the acoustic propagation in photoacoustic imaging, as corroborated by comparisons with k-Wave simulation results. Our forward model achieves the highest simulation accuracy among direct numerical methods by solving the wave equation using the pseudo-spectral method like k-Wave. Furthermore, the computational steps are completely differentiable, facilitating easy gradient propagation and parameter updates. It is worth noting that the multi-order spherical decomposition utilized in our differentiable rapid radiator is a general strategy, where specific decomposition approaches are not unique. The coefficients for the 10th-order spherical decomposition provided in the paper are empirical values for this order, which could be extended to higher orders to enhance model accuracy, albeit at the cost of increased computational

demand. Since comparisons with k-Wave have shown that the 10th-order precision is sufficient, all experiments in this paper are conducted under the condition of 10th-order decomposition.

Despite the significant advantages of SlingBAG in 3D photoacoustic reconstruction, there are certain limitations. When converting point cloud results to voxel grid results, especially with very sparse sensor data, there can be discontinuities in the voxel grid of vessels. This stems from the fact that converting point clouds to voxel grids is entirely based on our physical forward model. With insufficient sensor data, the densification of point clouds may fail to converge accurately in some areas, leading to sparseness, which ultimately results in discontinuities in the voxel grid vascular image. To address this issue, future work will incorporate physical constraint regularization on the point cloud data and perform surface alignment and smoothing of point clouds after iteration, drawing on methods related to 3D Gaussian splatting, to achieve better voxel grid results in 3D reconstructions.

Additionally, our SlingBAG reconstruction algorithm currently is only valid in a homogeneous, non-viscous medium. However, in reality of in vivo study, the heterogeneity of sound speed distribution is not always negligible. We will study this in future work. Preliminary solutions include: (1) Partitioning the reconstruction space according to sound speed distribution based on prior knowledge and using different sound speeds for the sources in different regions in the differentiable radiator; (2) Introducing a learnable parameter, sound speed v_s , for each point in the point cloud, where each point will form a sphere with a radius a_0 , defined by its resolution parameter a_0 , encompassing a uniform sound speed v_s within the sphere. This approach incorporates sound speed as an additional parameter in the iterative optimization.

Since the differentiable radiator in our SlingBAG algorithm is based on a multi-order spherical decomposition strategy in 3D space, it is currently not suited for 2D PAI. However, extending the SlingBAG algorithm to linear US array configurations is feasible. This would involve using multiple concentric disk analytical solutions to fit the forward propagation results of 2D point acoustic sources, similar to the 3D strategy, resulting in 2D planes of point clouds rather than 3D spaces. Given that sensor sparsity issues primarily arise in 3D array configurations for 3D photoacoustic imaging, we have not focused extensively on PAT in this paper, but we will explore this further in future work.

6 Conclusion

To the best of our knowledge, it is the first work in the field of 3D photoacoustic imaging reconstruction storing photoacoustic source information in the form of point clouds rather than voxel grids to perform iterative reconstruction. It achieves large-scale 3D photoacoustic iterative reconstruction ($40 \text{ mm} \times 104 \text{ mm} \times 80 \text{ mm}$) by directly optimizing the point cloud distribution from raw photoacoustic signals to reconstruct high-quality 3D results. The proposed SlingBAG 3D reconstruction algorithm is inspired by differentiable rendering techniques in computer graphics, introducing the concept of "differentiable radiation" for the first time. This allows for a high-precision forward propagation process and ultra-fast gradient back-propagation and parameter optimization during iterations. The algorithm achieves high-quality 3D reconstructions with sparse sensor distributions for both simulated hand vessels data and real mouse brain data, outperforming traditional iterative reconstruction algorithms in terms of reconstruction scale and speed.

Our SlingBAG algorithm is versatile, unaffected by the configuration of the detectors. It can be easily applied to any array shapes such as planar arrays and spherical arrays, making it a universal and generalizable 3D photoacoustic reconstruction algorithm. The differentiable rapid radiator based on multi-order spherical decomposition can also be used for photoacoustic forward process simulations in homogeneous, non-media. It achieves over 99.5% similarity with k-Wave simulation results and accelerates the simulation process by more than ten thousand times, making it efficient to perform forward process simulation in homogeneous and non-viscous medium.

In the future, we plan to extend the SlingBAG reconstruction algorithm to 3D photoacoustic reconstructions in media with heterogeneity sound speeds and attenuation. Additionally, we aim to expand its application range from non-focused arrays to focused transducer arrays, such as medical handheld probes, for photoacoustic reconstruction.

Acknowledgments

This research was supported by the following grants: the National Key R&D Program of China (No. 2023YFC2411700, No. 2017YFE0104200); the Beijing Natural Science Foundation (No. 7232177); the Basic Science Research Program through the National Research Foundation of Korea (NRF) funded by the Ministry of Education (2020R1A6A1A03047902).

We would like to express our gratitude to Professor Chao Tian and his student Zhijian Tan from the University of Science and Technology of China for their selfless support.

References

- [1] Y. Matsumoto, Y. Asao, A. Yoshikawa, H. Sekiguchi, M. Takada, M. Furu, S. Saito, M. Kataoka, H. Abe, T. Yagi, *et al.*, “Label-free photoacoustic imaging of human palmar vessels: a structural morphological analysis,” *Scientific reports*, vol. 8, no. 1, p. 786, 2018.
- [2] Y. Matsumoto, Y. Asao, H. Sekiguchi, A. Yoshikawa, T. Ishii, K.-i. Nagae, S. Kobayashi, I. Tsuge, S. Saito, M. Takada, *et al.*, “Visualising peripheral arterioles and venules through high-resolution and large-area photoacoustic imaging,” *Scientific reports*, vol. 8, no. 1, p. 14930, 2018.
- [3] I. Ivankovic, E. Merčep, C.-G. Schmedt, X. L. Deán-Ben, and D. Razansky, “Real-time volumetric assessment of the human carotid artery: handheld multispectral optoacoustic tomography,” *Radiology*, vol. 291, no. 1, pp. 45–50, 2019.
- [4] X. L. Deán-Ben and D. Razansky, “Portable spherical array probe for volumetric real-time optoacoustic imaging at centimeter-scale depths,” *Optics express*, vol. 21, no. 23, pp. 28062–28071, 2013.
- [5] K. Nagae, Y. Asao, Y. Sudo, N. Murayama, Y. Tanaka, K. Ohira, Y. Ishida, A. Otsuka, Y. Matsumoto, S. Saito, *et al.*, “Real-time 3d photoacoustic visualization system with a wide field of view for imaging human limbs,” *F1000Research*, vol. 7, 2018.
- [6] W. Kim, W. Choi, J. Ahn, C. Lee, and C. Kim, “Wide-field three-dimensional photoacoustic/ultrasound scanner using a two-dimensional matrix transducer array,” *Optics Letters*, vol. 48, no. 2, pp. 343–346, 2023.
- [7] D. Piras, W. Xia, W. Steenbergen, T. G. Van Leeuwen, and S. Manohar, “Photoacoustic imaging of the breast using the twente photoacoustic mammoscope: present status and future perspectives,” *IEEE Journal of Selected Topics in Quantum Electronics*, vol. 16, no. 4, pp. 730–739, 2009.
- [8] M. Heijblom, D. Piras, W. Xia, J. Van Hespren, J. Klaase, F. Van den Engh, T. Van Leeuwen, W. Steenbergen, and S. Manohar, “Visualizing breast cancer using the twente photoacoustic mammoscope: what do we learn from twelve new patient measurements?,” *Optics express*, vol. 20, no. 11, pp. 11582–11597, 2012.
- [9] S. Li, G. Zhang, Y. Wang, W. Li, Y. Sun, and C. Li, “Photoacoustic imaging of peripheral vessels in extremities by large-scale synthetic matrix array,” *Journal of Biomedical Optics*, vol. 29, no. S1, pp. S11519–S11519, 2024.
- [10] Y. Wang and C. Li, “Comprehensive framework of gpu-accelerated image reconstruction for photoacoustic computed tomography,” *Journal of Biomedical Optics*, vol. 29, no. 6, pp. 066006–066006, 2024.
- [11] K. Wang, R. Su, A. A. Oraevsky, and M. A. Anastasio, “Investigation of iterative image reconstruction in three-dimensional optoacoustic tomography,” *Physics in Medicine & Biology*, vol. 57, no. 17, p. 5399, 2012.
- [12] R. Shang, R. Archibald, A. Gelb, and G. P. Luke, “Sparsity-based photoacoustic image reconstruction with a linear array transducer and direct measurement of the forward model,” *Journal of biomedical optics*, vol. 24, no. 3, pp. 031015–031015, 2019.
- [13] J. Zhu, N. Huynh, O. Ogunlade, R. Ansari, F. Lucka, B. Cox, and P. Beard, “Mitigating the limited view problem in photoacoustic tomography for a planar detection geometry by regularized iterative reconstruction,” *IEEE Transactions on Medical Imaging*, vol. 42, no. 9, pp. 2603–2615, 2023.
- [14] A. Hauptmann, F. Lucka, M. Betcke, N. Huynh, J. Adler, B. Cox, P. Beard, S. Ourselin, and S. Arridge, “Model-based learning for accelerated, limited-view 3-d photoacoustic tomography,” *IEEE transactions on medical imaging*, vol. 37, no. 6, pp. 1382–1393, 2018.
- [15] A. Hauptmann and B. Cox, “Deep learning in photoacoustic tomography: current approaches and future directions,” *Journal of Biomedical Optics*, vol. 25, no. 11, pp. 112903–112903, 2020.
- [16] W. Zheng, H. Zhang, C. Huang, V. Shijo, C. Xu, W. Xu, and J. Xia, “Deep learning enhanced volumetric photoacoustic imaging of vasculature in human,” *Advanced Science*, vol. 10, no. 29, p. 2301277, 2023.
- [17] B. Mildenhall, P. P. Srinivasan, M. Tancik, J. T. Barron, R. Ramamoorthi, and R. Ng, “Nerf: Representing scenes as neural radiance fields for view synthesis,” *Communications of the ACM*, vol. 65, no. 1, pp. 99–106, 2021.
- [18] T. Müller, A. Evans, C. Schied, and A. Keller, “Instant neural graphics primitives with a multiresolution hash encoding,” *ACM transactions on graphics (TOG)*, vol. 41, no. 4, pp. 1–15, 2022.
- [19] A. Chen, Z. Xu, A. Geiger, J. Yu, and H. Su, “Tensorf: Tensorial radiance fields,” in *European conference on computer vision*, pp. 333–350, Springer Nature Switzerland Cham, 2022.
- [20] B. Kerbl, G. Kopanas, T. Leimkühler, and G. Drettakis, “3d gaussian splatting for real-time radiance field rendering,” *ACM Transactions on Graphics*, vol. 42, July 2023.

- [21] B. Yao, Y. Zeng, H. Dai, Q. Wu, Y. Xiao, F. Gao, Y. Zhang, J. Yu, and X. Cai, “Sparse-view signal-domain photoacoustic tomography reconstruction method based on neural representation,” *arXiv preprint arXiv:2406.17578*, 2024.
- [22] G. Paltauf, J. Viator, S. Prah, and S. Jacques, “Iterative reconstruction algorithm for optoacoustic imaging,” *The Journal of the Acoustical Society of America*, vol. 112, no. 4, pp. 1536–1544, 2002.
- [23] C. Huang, K. Wang, L. Nie, L. V. Wang, and M. A. Anastasio, “Full-wave iterative image reconstruction in photoacoustic tomography with acoustically inhomogeneous media,” *IEEE transactions on medical imaging*, vol. 32, no. 6, pp. 1097–1110, 2013.
- [24] S. R. Arridge, M. M. Betcke, B. T. Cox, F. Lucka, and B. E. Treeby, “On the adjoint operator in photoacoustic tomography,” *Inverse Problems*, vol. 32, no. 11, p. 115012, 2016.
- [25] S. Arridge, P. Beard, M. Betcke, B. Cox, N. Huynh, F. Lucka, O. Ogunlade, and E. Zhang, “Accelerated high-resolution photoacoustic tomography via compressed sensing,” *Physics in Medicine & Biology*, vol. 61, no. 24, p. 8908, 2016.
- [26] S. Weiss and R. Westermann, “Differentiable direct volume rendering,” *IEEE Transactions on Visualization and Computer Graphics*, vol. 28, no. 1, pp. 562–572, 2021.
- [27] L. Yariv, J. Gu, Y. Kasten, and Y. Lipman, “Volume rendering of neural implicit surfaces,” *Advances in Neural Information Processing Systems*, vol. 34, pp. 4805–4815, 2021.
- [28] J. T. Barron, B. Mildenhall, M. Tancik, P. Hedman, R. Martin-Brualla, and P. P. Srinivasan, “Mip-nerf: A multiscale representation for anti-aliasing neural radiance fields,” in *Proceedings of the IEEE/CVF international conference on computer vision*, pp. 5855–5864, 2021.
- [29] Y. Yao, J. Zhang, J. Liu, Y. Qu, T. Fang, D. McKinnon, Y. Tsin, and L. Quan, “Neilf: Neural incident light field for physically-based material estimation,” in *European Conference on Computer Vision*, pp. 700–716, Springer, 2022.
- [30] S. Fridovich-Keil, A. Yu, M. Tancik, Q. Chen, B. Recht, and A. Kanazawa, “Plenoxels: Radiance fields without neural networks,” in *Proceedings of the IEEE/CVF conference on computer vision and pattern recognition*, pp. 5501–5510, 2022.
- [31] B. Kerbl, G. Kopanas, T. Leimkühler, and G. Drettakis, “3d gaussian splatting for real-time radiance field rendering,” *ACM Trans. Graph.*, vol. 42, no. 4, pp. 139–1, 2023.
- [32] M. Zwicker, H. Pfister, J. Van Baar, and M. Gross, “Ewa splatting,” *IEEE Transactions on Visualization and Computer Graphics*, vol. 8, no. 3, pp. 223–238, 2002.
- [33] B. E. Treeby and B. T. Cox, “k-wave: Matlab toolbox for the simulation and reconstruction of photoacoustic wave fields,” *Journal of biomedical optics*, vol. 15, no. 2, pp. 021314–021314, 2010.
- [34] M. Xu and L. V. Wang, “Universal back-projection algorithm for photoacoustic computed tomography,” *Physical Review E—Statistical, Nonlinear, and Soft Matter Physics*, vol. 71, no. 1, p. 016706, 2005.
- [35] Y. Hu, T.-M. Li, L. Anderson, J. Ragan-Kelley, and F. Durand, “Taichi: a language for high-performance computation on spatially sparse data structures,” *ACM Transactions on Graphics (TOG)*, vol. 38, no. 6, p. 201, 2019.
- [36] S. Choi, J. Yang, S. Y. Lee, J. Kim, J. Lee, W. J. Kim, S. Lee, and C. Kim, “Deep learning enhances multiparametric dynamic volumetric photoacoustic computed tomography in vivo (dl-pact),” *Advanced Science*, vol. 10, no. 1, p. 2202089, 2023.
- [37] W. Choi, B. Park, S. Choi, D. Oh, J. Kim, and C. Kim, “Recent advances in contrast-enhanced photoacoustic imaging: overcoming the physical and practical challenges,” *Chemical Reviews*, vol. 123, no. 11, pp. 7379–7419, 2023.
- [38] J. Kim, J. Lee, S. Choi, H. Lee, J. Yang, H. Jeon, M. Sung, W. J. Kim, and C. Kim, “3d multiparametric photoacoustic computed tomography of primary and metastatic tumors in living mice,” *ACS nano*, 2024.
- [39] J. Kim, G. Kim, L. Li, P. Zhang, J. Y. Kim, Y. Kim, H. H. Kim, L. V. Wang, S. Lee, and C. Kim, “Deep learning acceleration of multiscale superresolution localization photoacoustic imaging,” *Light: science & applications*, vol. 11, no. 1, p. 131, 2022.
- [40] J. Park, S. Choi, F. Knieling, B. Clingman, S. Bohndiek, L. V. Wang, and C. Kim, “Clinical translation of photoacoustic imaging,” *Nature Reviews Bioengineering*, in press.